ARTICLES
https://doi.org/10.1038/s41550-020-1199-8

nature astronomy

Reconnection nanojets in the solar corona

Patrick Antolin[1,2]✉, Paolo Pagano[2], Paola Testa[3], Antonino Petralia[4] and Fabio Reale[4,5]

The solar corona is shaped and mysteriously heated to millions of degrees by the Sun's magnetic field. It has long been hypothesized that the heating results from a myriad of tiny magnetic energy outbursts called nanoflares, driven by the fundamental process of magnetic reconnection. Misaligned magnetic field lines can break and reconnect, producing nanoflares in avalanche-like processes. However, no direct and unique observations of such nanoflares exist to date, and the lack of a smoking gun has cast doubt on the possibility of solving the coronal heating problem. From coordinated multi-band high-resolution observations, we report on the discovery of very fast and bursty nanojets, the telltale signature of reconnection-based nanoflares resulting in coronal heating. Using state-of-the-art numerical simulations, we demonstrate that the nanojet is a consequence of the slingshot effect from the magnetically tensed, curved magnetic field lines reconnecting at small angles. Nanojets are therefore the key signature of reconnection-based coronal heating in action.

Magnetic reconnection in the solar corona relies on the slow photospheric granulation that quasi-steadily stresses the magnetic field to produce twisted and braided structures. Decades ago, Parker[1] described the reconnection scenario and proposed that coronal loops, the building blocks of the solar corona, would form through myriad tiny reconnection processes in the small misalignments of the braided field lines, each releasing a small amount of energy that is rapidly redistributed by thermal conduction along the reconnected field[2,3]. These tiny outbursts of energy were termed nanoflares—intensity bursts on the order of 10^{24} erg (approximately nine orders of magnitude lower than solar flares). This dissipative process goes hand-in-hand with reconnection outflow jets, corresponding to the bidirectional ejection of plasma and plasmoids from the reconnection point, accelerated by the release of magnetic tension to Alfvénic speeds[4–6].

Localized, low-intensity bursts in the nanoflare range associated with coronal heating have been observed in high-resolution extreme ultraviolet (EUV)[7,8], UV[9–11] and visible observations (for example, ref. [12]). Non-flare related, high temperatures of 10 million degrees have also been indirectly inferred in X-ray observations of coronal loops and attributed to nanoflares[13]. However, no reports have been able to directly link and unequivocally associate a coronal nanoflare-like intensity burst with a magnetic reconnection event leading to coronal heating, as initially proposed by Parker. This challenge has been considered unfeasible as the dissipation scales of the current sheets where reconnection occurs are impossible to detect. Moreover, despite initially being attributed solely to reconnection, nanoflare-like intensity bursts have since been obtained in non-reconnection-based numerical models, such as wave heating[14,15], leading to a lack of a direct observational diagnostic allowing coronal heating mechanisms to be differentiated at the smallest discernible scales.

Observational evidence for magnetic reconnection in the solar corona has instead been provided based on large-scale changes in the magnetic field following reconnection, large plasmoids in long current sheets typical of solar flares or in filament eruptions[16], large-scale plasma outflow at Alfvénic speeds along the reconnected magnetic field[17–19], and at small-scales in low-lying photospheric[20] and chromospheric structures[21] often leading to field-aligned jets[22,23]. The absence of direct observational evidence of small-scale, in situ dissipation in the solar corona has cast doubt on the possibility of solving the coronal heating problem in the foreseeable future.

A collection of nanoflares (known as a nanoflare storm) due to reconnection could provide substantial coronal heating only if they are triggered once the stressed field loads enough free energy to heat the loop. A popular theory for the switch-on mechanism is the magnetohydrodynamics (MHD) avalanche model: the system reaches a critical state in which the local loss of equilibrium in an elemental loop structure (strand) propagates to the entire structure, producing a nanoflare storm that heats the entire loop[24–26]. To date, no reports exist of an MHD avalanche of nanoflares leading to the formation of a coronal loop.

Analysis

In this work, we report the discovery of nanojets, a reconnection-based nanoflare signature that accompanies the coronal heating process of a loop to multi-million-degree temperatures, building a multi-wavelength band coherent scenario. The spatial and temporal evolution of the heating events and the dynamics of the braided loop structure bear characteristics that can be attributed to an MHD avalanche.

Coordinated observations with the Atmospheric Imaging Assembly (AIA)[27] of the Solar Dynamics Observatory (SDO), the Interface Region Imaging Spectrograph (IRIS)[28] and the Hinode/Solar Optical Telescope (SOT)[29,30] were carried out on 3 April 2014 with target a loop-like structure at the limb of the Sun. The loop presented a dip at the apex, hosting a high-standing prominence at a height of 20,000 km to 40,000 km (see Fig. 1). From the top of the structure, the material flowed as coronal rain along curved paths to the solar surface continuously for several hours, allowing the dynamic and fine-scale tracing of the magnetic field. The off-limb observation presents a dark background to the loop structure and a sideways line of sight (LOS) to the loop plane[31]. This preferential configuration has allowed a clear distinction of the dynamics. Several rain strands were observed, particularly in the 2,796 Å and 1,400 Å slit-jaw imager (SJI) filters of IRIS, indicating temperatures from 10,000 K to 100,000 K (ref. [28]). The strands presented small apparent misalignments in the plane of the sky (POS) with

[1]Department of Mathematics, Physics and Electrical Engineering, Northumbria University, Newcastle Upon Tyne, UK. [2]School of Mathematics and Statistics, University of St Andrews, St Andrews, UK. [3]Harvard–Smithsonian Center for Astrophysics, Cambridge, MA, USA. [4]INAF–Osservatorio Astronomico di Palermo, Palermo, Italy. [5]Dipartimento di Fisica & Chimica, Università di Palermo, Palermo, Italy. ✉e-mail: patrick.antolin@northumbria.ac.uk

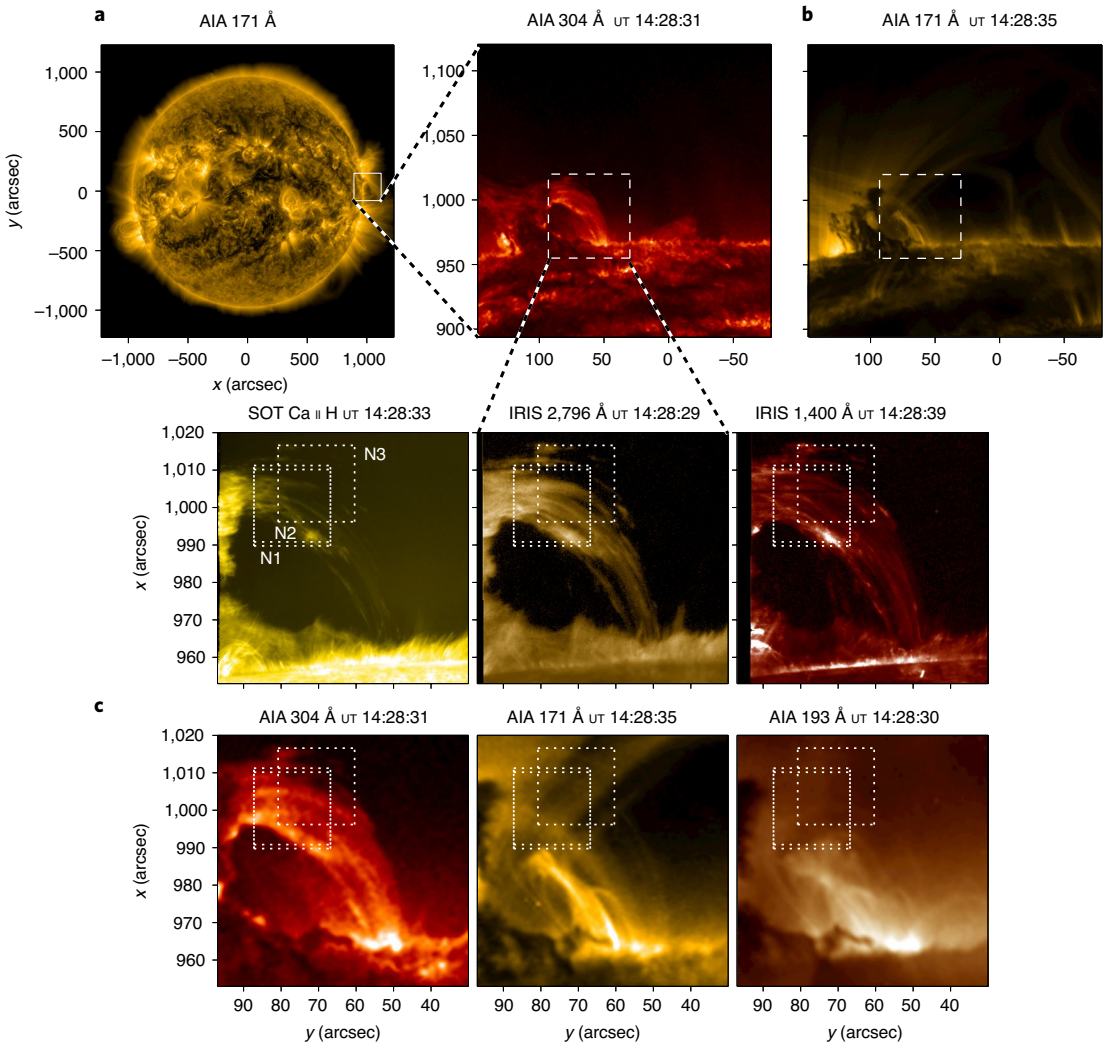

Fig. 1 | SDO, IRIS and Hinode co-observation of the coronal structure. a, Full-disk SDO/AIA image in the 171 Å channel of the Sun on 3 April 2014. **b**, Zoomed and rotated portion of the field of view (FOV) (white square on the West limb) in the AIA 304 Å and 171 Å channels. The IRIS/SJI FOV is indicated by the white dashed square. **c**, Top row, co-observed FOV between Hinode/SOT (left, in the Ca II H line) and IRIS/SJI (right, in the 2,796 Å and 1,400 Å channels, respectively). The visible loop-like coronal structure is the subject of this study. A radial filter has been applied to decrease the intensity of the solar disk and to make the off-limb features more visible. Bottom row, the corresponding AIA images for the Hinode and IRIS FOV in the AIA 304 Å, 171 Å and 193 Å channels from left to right. The main structure of interest is the loop-like structure connecting the prominence (bright structure to the left in the SOT FOV) to the solar surface. The three dotted rectangles N1, N2 and N3 in **c** correspond to the FOVs of Figs. 2, 3 and 4, respectively. The time that images were captured at is given above as universal time (UT; h:min:s).

maximum angles of $25 \pm 5°$. The EUV absorption from the rain suggests densities of 1.6×10^{10}–1.6×10^{11} cm^{-3}, typical of coronal rain[32] (Supplementary Information). The loop structure was initially only dimly visible in the EUV 171 Å channel of AIA, indicating mild heating to temperatures around 700,000 K.

The focus of this work is on the last 30 min of observation. The loop started an accelerated and differential expansion up to 15 km s^{-1}, with the apex moving outwards while the visible footpoint remained mostly static. Before and, in particular, during the expansion, small and localized intensity bursts are observed in the rain strands. The bursts are accompanied by jet-like structures perpendicular to the rain strands with total speeds of a few hundreds of kilometres per second, followed by rapid outward transverse displacements and rotational motions of the strands up to 60 km s^{-1} (Figs. 2 and 3, see also Extended Data Figs. 1 and 2 and Supplementary Figs. 2–9). These jets, which we term nanojets, are best visible in the transition region IRIS 1,400 Å channel, they have EUV signatures in most AIA channels and present almost no signature in the chromospheric IRIS 2,796 Å channel (Extended Data Figs. 3 and 4 and Supplementary Figs. 10–12). They have widths on the order of 500 km, lengths of 1,000–2,000 km and are extremely short lived (~ 15 s or less). Most are only visible for one snapshot in IRIS 1,400 Å, but can be followed at higher cadence with AIA, indicating POS speeds of 100–200 km s^{-1}. The most prominent set of nanojets occurs at the beginning of the expansion. The set is highly clustered near the apex, at the lower part of the loop, with some nanojets separated by 1 arcsec or less (Fig. 2). The episode lasts about 100 s and brings the greatest morphological change within the loop. Subsequently, other nanojets appear throughout the loop, some occurring in clusters and others in apparent isolation (Fig. 3). The largest events involve the ejection of plasmoids along the jets axis with widths on the order of 1 arcsec at speeds in the POS of 50–60 km s^{-1} (Fig. 2). Several nanojets were captured by the spectrograph of IRIS and show a LOS velocity component in the Mg II and Si IV lines with a magnitude

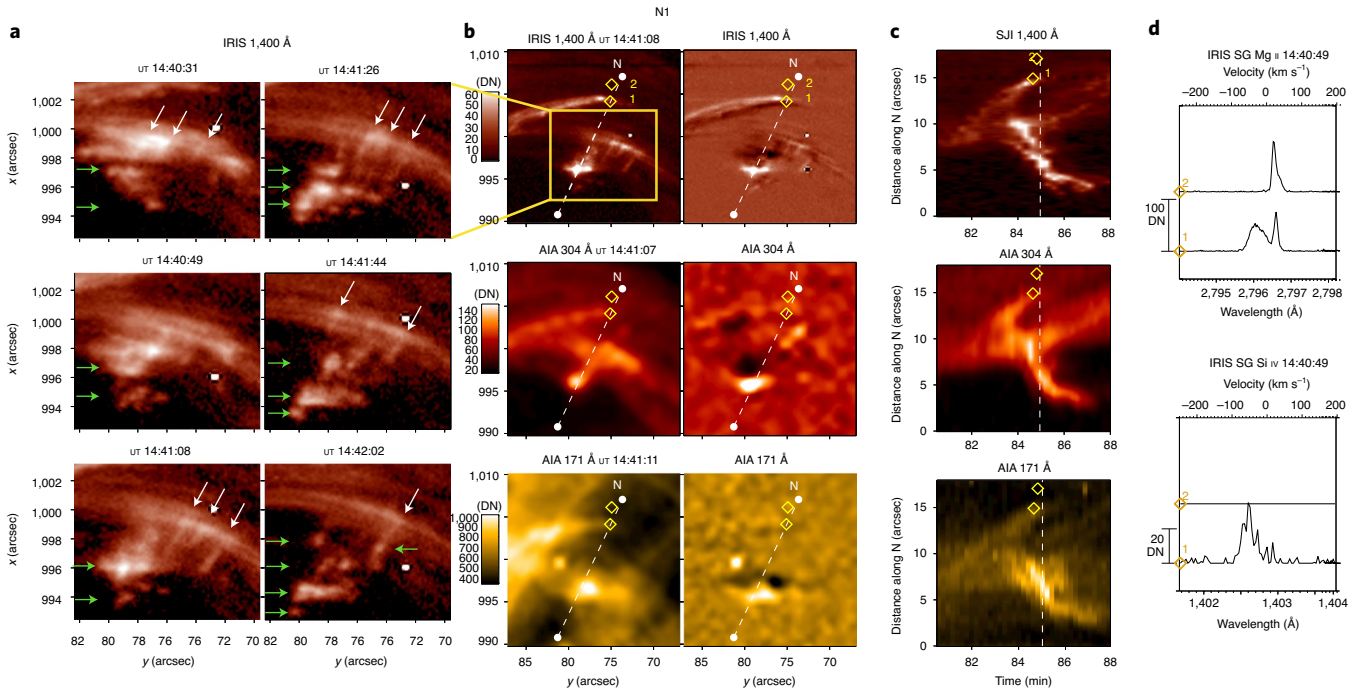

Fig. 2 | A nanojet cluster with plasmoid ejecta. a, A snapshot sequence (time points are indicated at the top of each image) of a nanojet cluster in the IRIS 1,400 Å of a zoomed-in region of **b**. Note the tight clustering of the nanojets (white arrows) and the ejection of plasmoid-like structures from the cluster (green arrows). **b**, FOV marked N1 in Fig. 1, showing a snapshot of the nanojet cluster (left) and its running difference version (right). From top to bottom: the IRIS 1,400 Å, AIA 304 Å and AIA 171 Å channels, respectively. The unit of intensity is data numbers (DN), proportional to the number of photons (~ 1, 12 and 18 photons per DN, respectively, for the AIA channels, IRIS 1,400 Å and 2,796 Å). **c**, Time–distance diagrams along cut N (white dashed lines). The time of the snapshot in **b** is indicated by the white vertical dashed line. The time is measured from the start of the IRIS observation. **d**, The IRIS spectrograph (SG) captures part of the process: a strand is displaced upwards simultaneously with the ejecta and at similar speeds. The two yellow diamonds in the IRIS 1,400 Å images of **b** show slit locations 1 and 2 (corresponding to the raster position number) along cut N, and their spectra in the Mg II k 2,796.0 Å and Si IV 1,402.77 Å lines are shown, respectively, in the top and bottom panels of **d** (for the spectrograph we have 4 and 18 photons per DN for Si IV and Mg II lines, respectively). We select the pixel with the brightest integrated intensity within a four-pixel distance from cut N along the slit. See Supplementary Video 1.

above 100 km s^{-1} and with a spectral line broadening due to unresolved (that is, non-thermal) velocities of similar magnitude; there is also an up to 15-fold increase in the Si IV line integrated intensity with respect to the average (for example, Fig. 4 and Table 1). We note that the determination of multiple components in the line profiles is relatively straightforward owing to the off-limb viewpoint and to the low optical thickness of the rain emission (see Methods).

The spatial distribution of the nanojets spreads out across (inward to outward) and along the loop, with some occurring just above spicular heights (Extended Data Fig. 5). Their occurrence also increases with time (Extended Data Fig. 6). In the 13 min time span of their occurrence, we estimate the number of resolved nanojets to be on the order of 150 (Extended Data Fig. 7, see Methods). The nanojets precede the formation of coronal strands (Extended Data Fig. 5), which become visible in most EUV wavelengths (for example, Extended Data Figs. 4 and 8). These are formed locally first, before encompassing (and thereby forming) the coronal loop. The temporal and spatial evolution of the nanojets, the intensity bursts and overall increase in EUV intensity are thus highly suggestive of an MHD avalanche. A differential emission measure (DEM) analysis of the loop with the AIA channels indicates temperatures of 2–5 MK, with possible maxima up to 10 MK (Extended Data Fig. 9). The rain strands become more parallel to each other through time in the POS (Extended Data Fig. 10), and show internal rotational motion at speeds of 50 km s^{-1}, counter-streaming flows along the loop and non-thermal line broadening both up to 80 km s^{-1} (Supplementary Fig. 13). This is strongly indicative of a reduction in the braiding and of untwisting, which are expected in MHD avalanche models (for example, ref. [33]). The dissipated energy per nanojet is estimated to be up to 10^{25} erg (Methods), with the bulk of the distribution probably being out of reach of the present instrumentation.

To confirm that nanojets with the observed characteristics are indeed possible through reconnection at small-angle magnetic field misalignments and to further examine their nature, we conduct a 3D MHD experiment with two slightly misaligned flux tubes reconnecting at one point in the corona (Methods). A highly localized reconnection event is obtained that satisfactorily explains the nanojet as one of the bidirectional reconnection outflows and accompanying field line displacement accelerated by magnetic tension (Fig. 5). The strongest dynamics (which make up the nanojets) come from the perpendicular advection of the field lines from the reconnection site, with relatively small longitudinal (field-aligned) plasma velocity. Hence, contrary to most reconnection-based solar jets, which are usually rooted in the chromosphere (for example, ref. [23]), the small-angle coronal reconnection observed here does not involve a strong plasma flow along the reconnected field lines (Fig. 6). We observe a single nanojet mostly because in a curved loop the magnetic tension is substantially larger inwards than outwards (Supplementary Information). Besides the overall shape and the dynamics, our simulations also reproduce the local temperature increase and the larger-scale perpendicular displacement of the reconnecting field lines (which would characterize a strand in the presence of rain).

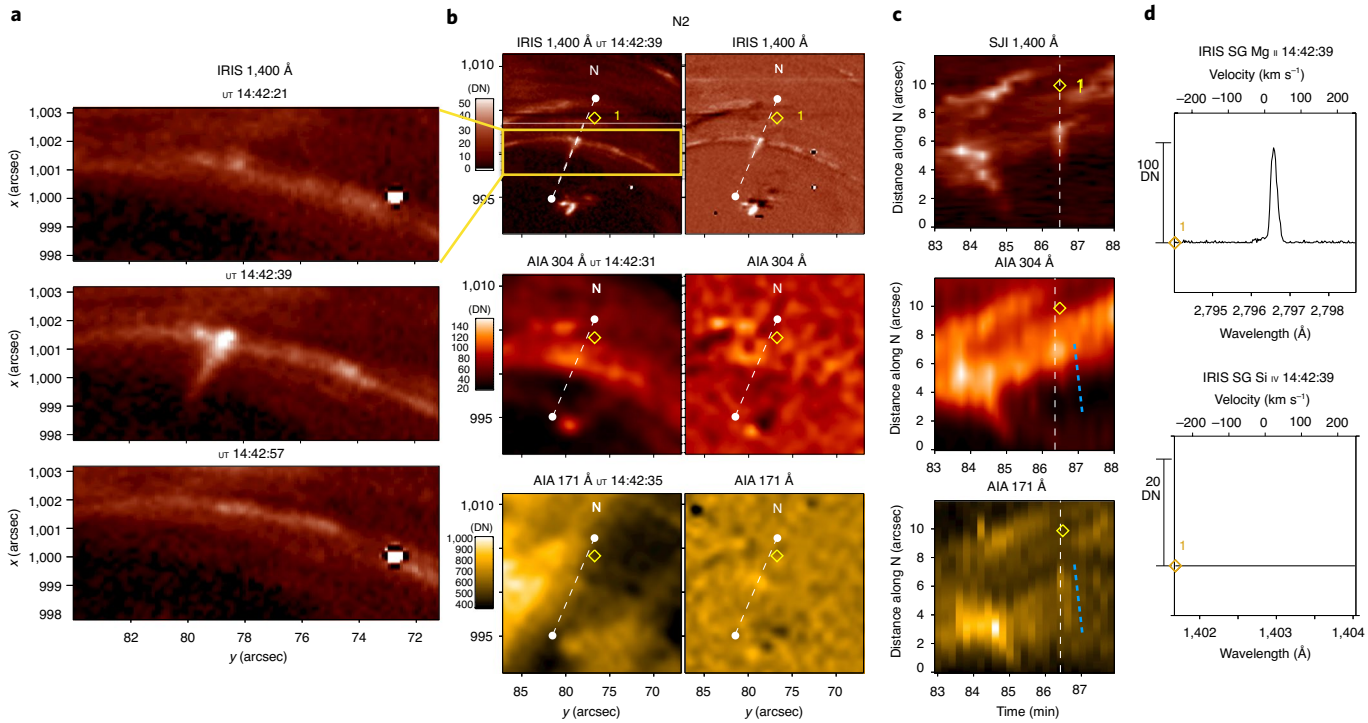

Fig. 3 | A single nanojet. a, A snapshot sequence in the IRIS 1,400 Å of a zoomed-in region in which a single nanojet can be seen. The nanojet is composed of a bright head stemming from a rain strand, a length of 2–3 arcsec and an average width of 500 km. The nanojet is only seen during one snapshot in IRIS 1,400 Å, but can be followed over a few snapshots in the AIA channels. **b**, Keeping the same panel configuration as in Fig. 2, the region marked N2 in Fig. 1 is shown here. **c**, The resulting vertical and slanted patterns in the time–distance plots for the IRIS and AIA images. The slope of the slanted pattern (blue dashed line) indicates a POS speed of ~240 km s^{-1}. **d**, The IRIS slit is too far from the nanojet and no associated feature can be seen in the spectra. See Supplementary Video 2.

There are many types of physical driver for magnetic reconnection, such as dynamic instabilities or the magnetic field shuffling from granular convection. The major nanojet episodes occur during loop expansion, and they are probably driven by the partial loss of equilibrium of the prominence at the top of the loop, as suggested by numerical modelling[34] (see Supplementary Information). Two other episodes of clustered nanojets are observed much earlier than the loop expansion, one in a different loop that may not be attached to the prominence (Supplementary Figs. 16–18). These episodes involve the same combination of features: the nanojets, localized intensity bursts and rapid displacement of strands. However, we only observe local variation without large-scale coronal strands, indicating an overall smaller energy release. We therefore suggest that the nanojet as a singular entity is largely independent of the nature of the driver. As we have shown, the morphology of the nanojets mostly depends on the (small-angle) magnetic reconnection in a strong guide field topology (such as a coronal loop). However, their numbers and evolution as a group (for instance, as an MHD avalanche) will be strongly dependent on the driver, as it defines the overall available energy.

Discussion

The heating events, the detailed dynamics and morphology, and particularly the details of the nanojets, constitute major challenges for reconnection-based numerical models and provide major constraints on the nature of reconnection in the solar corona. A major finding from these observations is the discrete and very distinct occurrence of the nanojets that, although numerous, appear as a countable phenomenon. This discrete nature may suggest that reconnection occurs episodically and strongly supports the reconnection-based nanoflare theory that nanoflares constitute elemental heating events that can be responsible for coronal heating. If reconnection were non-localized and continuously occurring along long current sheets, the nanojets and the accompanying intensity bursts would not be highly localized but would involve entire rain strands moving perpendicularly at Alfvénic speeds (producing a smeared image effect for the displaced rain strands), which is not observed. One possibility is that the rain plays an important role in the reconnection process. The partial ionization state of the rain means that ambipolar diffusion is more efficient, thereby facilitating reconnection[35]. However, not all of the observed nanojets seem to be rooted in cool and dense plasma, as the high-resolution Hinode/SOT observations indicate. Also, most nanojets cannot be seen in the chromospheric channels (see Methods). Lastly, as our three-dimensional MHD numerical experiment suggests, highly localized reconnection would happen even in the absence of partially ionized and clumpy plasma. This suggests that the rain is a backdrop against which the reconnection nanojets can be seen and may also be a catalyst of the process, but not a requirement.

Another theoretical challenge is the appearance of plasmoids accompanying the nanojets at large enough scales to be visible with the present instrumentation, suggesting that the magnetic islands involved in the secondary tearing mode instability can grow in non-flare related and small-scale current sheets. We therefore expect that the nanojets resolved here constitute the high end of the true distribution of spatial and energy scales involved in this reconnection scenario, so the bulk of the distribution has energies below 10^{25} erg, as predicted from theory[1]. Our results therefore strongly suggest that next-generation instrumentation will readily observe the distribution of scales of these events. The distinct observational signatures revealed here serve as a guide that allows heating mechanisms to be distinguished on the basis of magnetic

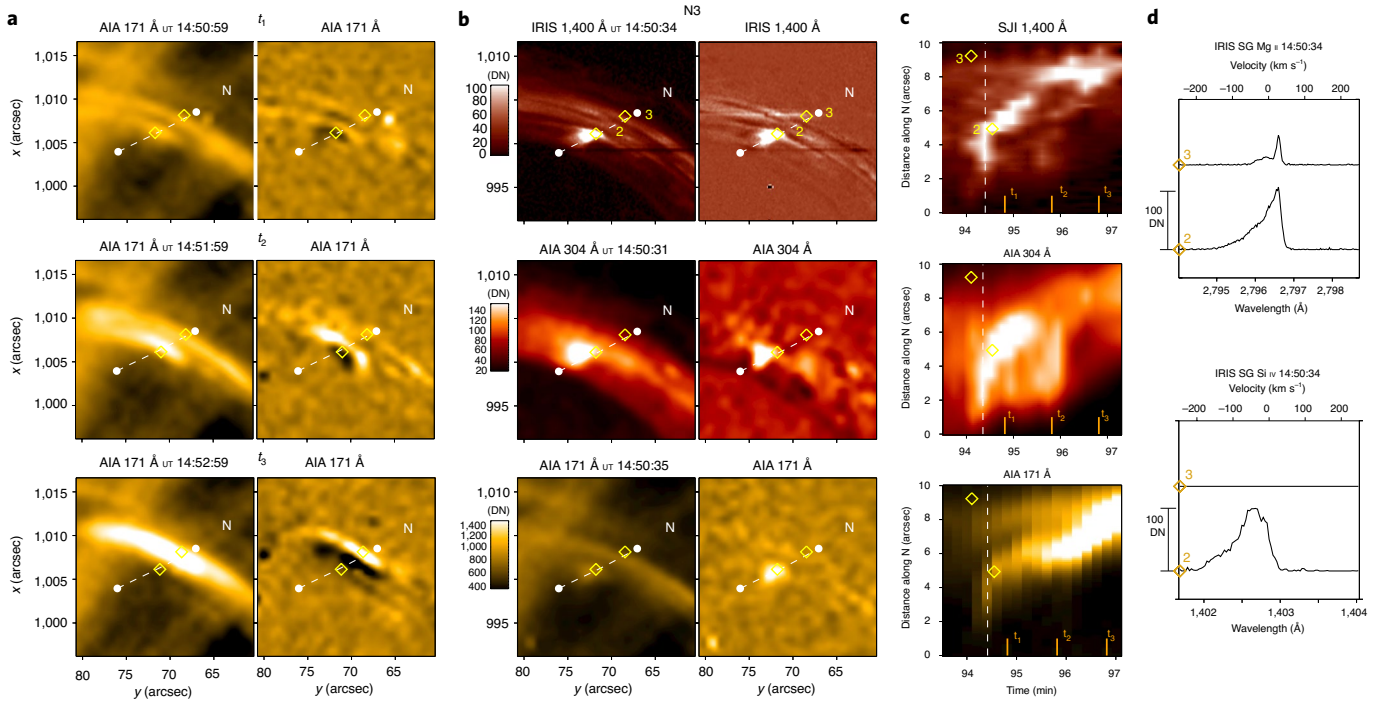

Fig. 4 | Spectral features of a nanojet and coronal loop formation. Keeping the same panel configuration as Fig. 2, we show here a nanojet fully captured by the IRIS slit. **a**, The AIA 171 Å snapshot pairs (of snapshot (left) and its running difference version (right)) for three instances in time labelled t_1, t_2 and t_3, each separated by 1 min. **b**, We show here a snapshot (left) with its running difference version (right) in the IRIS 1,400 Å (top), AIA 304 Å (middle) and AIA 171 Å (bottom) at a time 30 s prior to the sequence in **a**. **c**, Time–distance diagrams along cut N (white dashed lines in **b**) in each channel. The time of the snapshot in **b** is indicated by the white dashed vertical line. **d**, The Mg II k 2,796.0 Å (top) and Si IV 1,402.77 Å (bottom) spectral lines at slit locations 2 and 3 and time indicated in **b** (yellow diamonds). The localised brightening seen in **b** is accompanied by blueshifted material with Doppler speeds close to −200 km s^{-1} (particularly clear in the Si IV line). The strand then progressively brightens in the AIA 171 Å channel, extending upward and downward along the rain flow, as seen in **a**. At the same time, the strand is displaced transversely, upward along cut N, as shown in **c**. See Extended Data Fig. 5 for the full spatial extent of the coronal strands. See Supplementary Video 3.

Table 1 | Statistics based on Si IV spectra

		Quiet period (before expansion)	Nanojets
Number	Spectra	7,264	445
	Spectral components	7,326	751
Total intensity (DN)	Mean	146.2	410
	Standard deviation	28	223.4
∑|Doppler velocity| (km s^{-1})	Mean	15.8	103
	Standard deviation	10.4	36.6
|Doppler velocity| (km s^{-1})	Mean	15.6	61.2
	Standard deviation	13.3	31.4
$\sum\xi$ (km s^{-1})	Mean	23.1	47.4
	Standard deviation	8	13.3
ξ (km s^{-1})	Mean	23	28
	Standard deviation	8	14.6

ξ, non-thermal velocity. The sum symbol denotes a sum over all spectral components for each spectral profile.

reconnection, thus providing a clear target and path for next-generation high-resolution instrumentation to solve the coronal heating problem.

Methods

Spectral line fitting and statistical analysis. The Mg II k and Si IV 1,402.77 Å spectra from the rain present multiple components, and both broad and thin spectra. Most of the rain away from the prominence can be considered to be optically thin in Mg II k (see Supplementary information). A multiple Gaussian fitting was performed to retrieve the multiple components automatically at every pixel and for every time step. The fitting routine acts on the basis of various thresholds such as a large enough signal-to-noise (SNR) ratio and sufficient data points to fit individual profiles, and discards pixels hit by cosmic rays. First, a single Gaussian is fitted and the result is used as an initial guess for additional single and double Gaussian fits. The best fit is selected on the basis of the lowest sigma errors

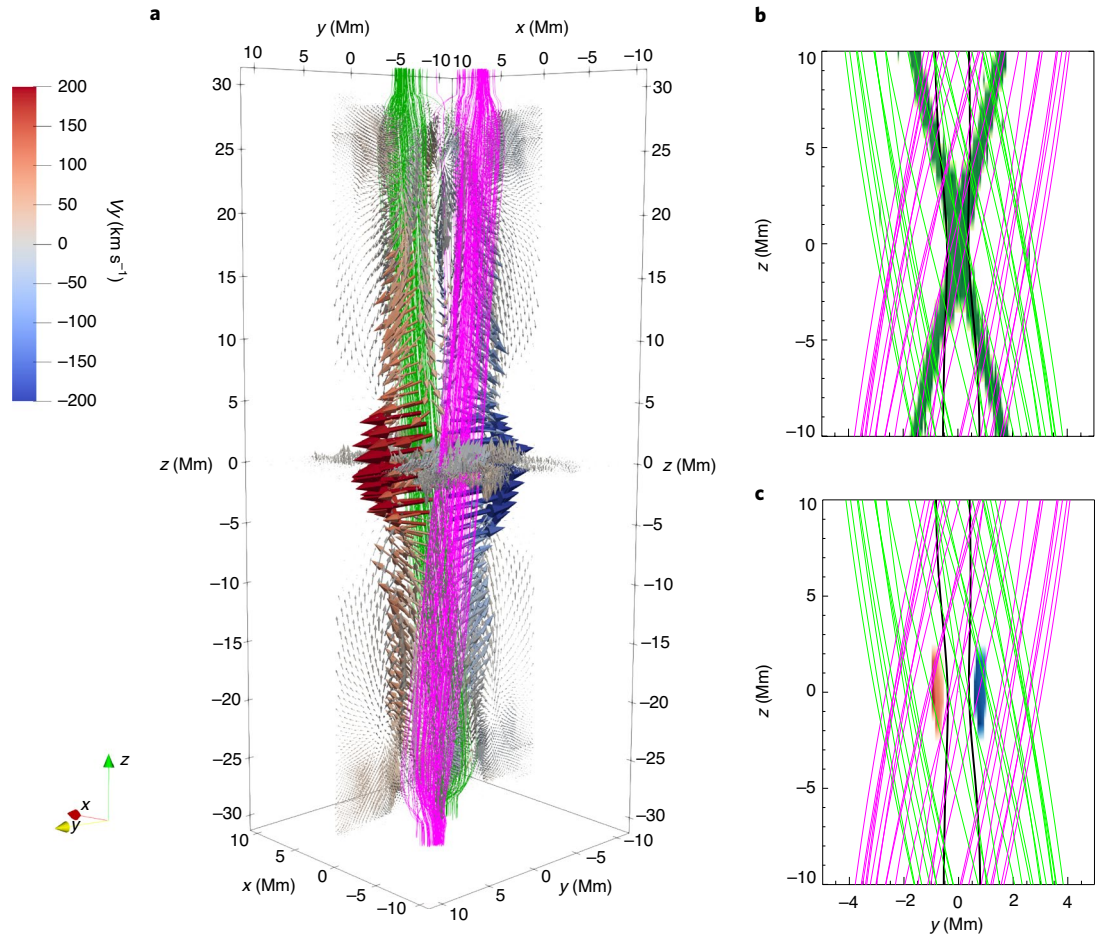

Fig. 5 | A nanojet in our numerical model. Magnetic field lines representative of the two loops (magenta and green) are displayed in all panels, as described in the Methods. **a**, Magnetic field lines in the 3D numerical box at the moment of the nanojet occurrence ($t = 420$ s). Magnetic reconnection is localized around $z = 0$. The magnetic tension from the reconnected magnetic field lines produces a high-velocity (up to 200 km s^{-1}), bidirectional jet collimated along the y axis. The widths of the region with high velocities (>100 km s^{-1}) along the x and z axes are less than 1 Mm and 3 Mm, respectively. Note also that the z velocities are only on the order of 20 km s^{-1}. The red–blue colour bar indicates the distribution of magnitude of the velocity vectors (in km s^{-1}), with grey indicating velocities around 0 km s^{-1}. **b**,**c**, The central region at $t = 380$ s, just before the nanojet, showing the isocontours of the electric current where $|J| = J_0$ (**b**, x-type green shaded region) and the isocontours of the y component of the velocity where $v_y = \pm 190$ km s^{-1} (**c**, blue and red shaded regions). Note how the regions of highest magnetic tension of the reconnected magnetic field lines (black) match the high-velocity region, resulting in the nanojet. See Supplementary Video 4.

and is then subtracted from the original spectral profile. More single Gaussian fits are performed on the residuals on the blue and red parts of the spectra to detect higher Doppler shifted components with high enough SNRs that are not captured by the first fits. In this way, a maximum of 4 possible components are allowed for each spectral profile. The fitting routine was checked by an extensive visual inspection on random locations in time and space. A total of roughly 120,000 fits were obtained for the Mg II line, with 60% found to be best represented by a single Gaussian with no other component. The rest was best represented with either a double Gaussian and/or a single Gaussian with additional Doppler components on the blue or red side of the spectrum. The Si IV spectra generally present a much lower SNR, leading to far fewer detections (11,000). A further check on the consistency of the results was then performed by spatially binning along the slit by three pixels and rerunning the analysis.

Statistical evolution of the nanojets' spectral properties. The Doppler and non-thermal velocities show a substantial variation during the expansion ($t = 84$–97 min) in both the Mg II k and Si IV 1,402.77 Å lines (Supplementary Fig. 13), with an increase in the Doppler velocities mainly towards the blue reaching speeds of 150 km s^{-1}, and a corresponding increase in the non-thermal velocities up to 80 km s^{-1}. The peak and integrated intensities increase by more than two orders of magnitude above the background noise in Si IV profiles, whereas the Mg II profiles have increased integrated intensities and reduced peaks, indicating heating of the initially cool material.

The observed properties of the jets indicate that we can define them on the basis of their dynamics and Si IV intensities. We define a jet as an event satisfying both a large enough integrated intensity in the Si IV line (set to 200 DN ≈ 1.4 times the average rain emission during the period before the loop expansion) and large enough summed Doppler and non-thermal velocities (where the sum occurs also over all spectral components, and we set this velocity threshold to 100 km s^{-1}). This choice is based on the distribution in total intensity and velocity of the IRIS spectra, shown in Extended Data Fig. 7. This nanojet definition is also supported by our numerical simulation results. We find 445 spectra (slit pixels) that satisfy these conditions, all during the last 4 min of observation (Extended Data Fig. 7 and Table 1). The nanojets appear as highly localized features along the slit (marked with arrows in Extended Data Fig. 7), first towards the apex and then expanding rapidly along and down the loop leg. Despite the countable nature observed in Figs. 2, 3 and 4 (and in Extended Data Figs. 1 and 2 and Supplementary Figs. 2–9, 16 and 17), determining the precise number of detected nanojets in this dataset is not straightforward, due to their tight clustering and very fast nature. Taking an average width of a nanojet of ~ 500 km and an average lifetime of 15 s (about ten measurements per nanojet with the IRIS slit, see Extended Data Fig. 7c), we estimate that 44 nanojets could have been captured by the IRIS slit. Assuming a constant occurrence rate over the time interval where they manifest, we estimate the total number of nanojets to be above 150. However, this is very likely a lower threshold given their clustering, avalanche-like occurrence and the limits of current detectability.

DEM analysis. The thermal evolution of the coronal plasma can be constrained by the AIA observations. Here we derive the DEM by applying the inversion method of ref. [36] to the time series of the coronal AIA passbands (see Supplementary

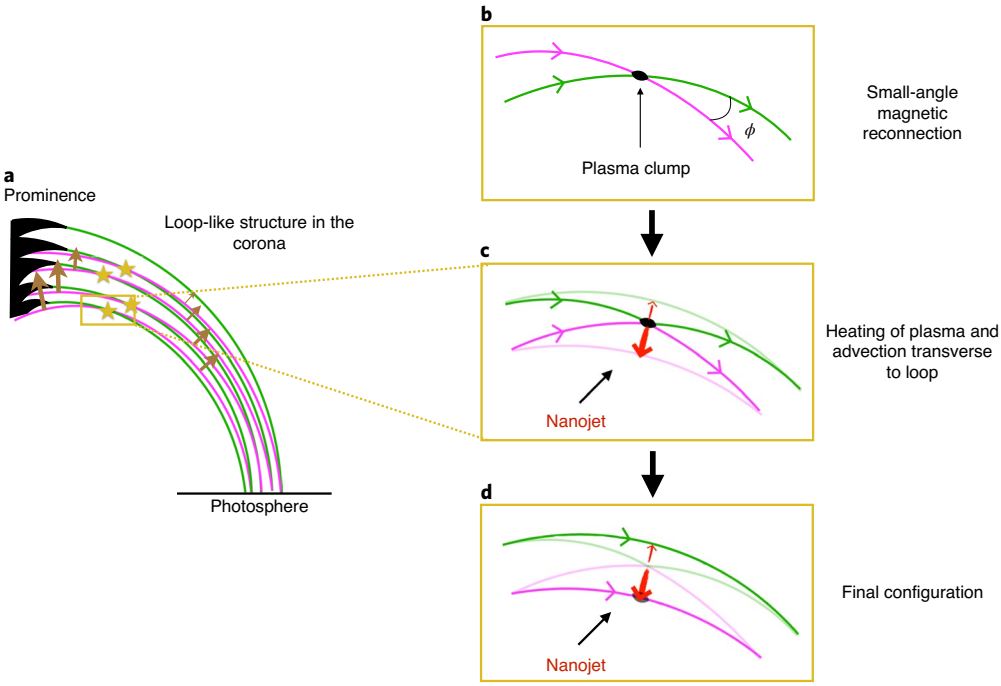

Fig. 6 | Sketch of a nanojet. a, Sketch of the loop-like structures observed in the POS. The brown arrows show the slow upward expansion of the loop apex. The stars denote the nanoflares, for which the evolution is shown in **b**, **c** and **d**. **b**, Small misalignments between the green and magenta field lines lead to reconnection at small angles ϕ. **c**, Plasma is heated and advected transversely to the loop at large speeds due to magnetic tension, thereby creating the nanojet. The inward component is much larger than the outward component (red arrows) due to the curved topology of the field lines, thus leading to the singular nature of the jet. **d**, A final configuration is reached with reduced braiding and misalignment between field lines at a higher temperature. A coronal strand starts to form.

information). The loop can be distinguished in the emission measure (EM) plots of Extended Data Fig. 9a in a wide range of temperatures, from $\log T = 5.5$ (corresponding to the cool EUV material surrounding the condensations) to $\log T = 6.7$ and possibly higher. The fact that the pixels along the loop consistently show the same temperature range provides support for the presence of these temperatures. The appearance of hot plasma emission in the loop ($\log T = 6.3 - 6.5$ and possibly higher) is demonstrated in the EM difference image (Extended Data Fig. 9b).

The observed loop strand in the EUV channel has an average thickness of 1,400 km. Taking a depth for the structure similar to that in the POS and average EM values of 10^{28}–$10^{28.7}$ cm^{-5}, we obtain electron number densities for the EUV emitting material in the range $8.5–19 \times 10^{9}$ cm^{-3}. The jets, having an average width of 500 km, have number densities in EUV in the range $1.4–3.1 \times 10^{10}$ cm^{-3}. Note that these densities are close, but smaller than the densities of the rain strands (Supplementary Information). It is likely that owing to their very small size, the jets fail to make a substantial deviation to higher EM values. This small difference can also be attributed to the compressibility of the plasma in the reconnection region. The fact that the nanojets are mostly absent in the IRIS 2,796 Å filter also supports a difference in density.

Evolution of braiding and twisting of the loop structure. The IRIS and Hinode observations show several coronal rain strands at high resolution crossing each other near the apex of the loop. The misalignment between the strands can be seen in Extended Data Fig. 10 and amounts to an apparent maximum in the POS of $25 \pm 5°$. The location of the crossing in the POS of strands near the apex seems to coincide with the first location of the nanojet occurrence, intensity brightening and plasmoid ejection. Previously redshifted downflowing plasma is replaced by rapidly evolving blueshifted strands moving at total speeds of ~60 km s^{-1} towards the apex of the loop. This motion is then replaced by consistently redshifted and blueshifted strands towards the end of the observation (see Extended Data Fig. 10g,h and the blue/red arrows in Supplementary Fig. 14) at the lowest and highest portions of the loop, respectively, suggesting an azimuthal motion (Supplementary Fig. 14) and a complex untwisting motion of the loop. At the same time, the loop structure expands and becomes thinner in all spectral channels, and the angle between the helical shape of strands and the loop axis is reduced to $10 \pm 3°$. These features suggest an overall reduction in the braiding of the loop (see Supplementary Video 9).

The nature of the nanojets. The dynamics of the nanojets can be understood through component magnetic reconnection between magnetic field lines from below the loop and the field lines connected to the prominence above (Supplementary information, Supplementary Fig. 15). In this scenario, the expected reconnection outflow is partly in the POS, being perpendicular to the rain strands, with a component along the LOS that is determined by the presence of shear and twist. Since the observed LOS velocity component of the jets is on the same order as the POS component, we expect a sheared component of the field of the same order as the misalignment in the POS (in the range 10–30°). We therefore interpret the nanojet as a part of the reconnection outflow, with magnetic tension being the driver of the observed dynamics. This kind of nanojet is different from the usual reconnection-driven jet concept in the sense that the observed outflow is not directed along the guide field. This is supported by the fact that both the nanojet axis and the ejected plasmoids are perpendicular to the loop (Fig. 2), and trace new, rapidly separating strands. Numerical work has shown that plasmoids produced by the tearing mode merge in the reconnection exhaust to form larger and slower plasmoids[37]. It is therefore likely that the observed plasmoids are part of the upper tail of the size and energy distribution for such reconnection events.

A peculiar aspect of the nanojets is that almost all point radially inwards with respect to the curvature of the loop (for an exception see nanojet N12, occurring further down the leg; Supplementary Fig. 8). This can be explained by the loop curvature, which implies that magnetic tension is expected to point mostly inwards. Taking a circular geometry, the ratio of inward to outward magnetic tension between two slightly misaligned strands can be as high as 100 with the high possibility of no outward component (and thus no outward jet). We therefore expect on average either only inward jets or inwards jets that are faster and longer than outward jets (and therefore more visible). Also, contrary to the inward jets, the outward jets (if any) have the loop as background emission and are therefore much harder to detect. In this case, as all inward jets are mostly blueshifted, we expect the respective outward components to be redshifted. This is supported by the presence of redshifted secondary components for some nanojets (as seen in Extended Data Fig. 2 and Supplementary Fig. 5) and the fact that the non-thermal broadening of the jet spectra is of the same order of magnitude as their Doppler shifts.

Reports of other jets in the solar corona exist[18,38], exhibiting a transverse morphology to the coronal structures and an episodic and singular nature (that is, non-bidirectional). Their generation mechanism could share common features with that of the nanojets, although the other jets involve different topologies and an energy range considerably higher than those observed in the nanojet and nanoflare scenario.

Energetics. We can estimate the rate of kinetic and thermal energy outflow in the nanojet on the basis of the observed characteristics. We can further estimate

the total energy liberated during a single event. Taking a representative total outflow speed of $v_o = 100\,\mathrm{km\,s^{-1}}$, inflow densities determined by EUV absorption of $\rho_i = (1.6\times10^{10}–1.6\times10^{11})\,\mathrm{cm^{-3}}$, outflow densities determined by DEM analysis of $\rho_o = (1.4–3.1)\times10^{10}\,\mathrm{cm^{-3}}$, an outflow width ℓ on the same order as the width of the nanojet (with a representative value of $\ell = 500\,\mathrm{km}$) and an average temperature of 2 MK, we obtain an outflow kinetic energy rate of $(5.8\times10^{14}–1.29\times10^{15})\,\mathrm{erg\,cm^{-1}\,s^{-1}}$ and an outflow thermal energy rate of $(2.9\times10^{15}–6.4\times10^{15})\,\mathrm{erg\,cm^{-1}\,s^{-1}}$. Taking a representative time span of 15 s and a representative length of 1,500 km, we estimate the total energy released by a nanojet to be $(7.8–17.3)\times10^{24}$ erg. We expect that the observed range of energies corresponds to the high end of the nanojet distribution, most of which is likely to be unresolved by the present observations.

Numerical modelling of nanojets. To better understand the dynamics of the nanojet generation in the solar corona, we devise non-ideal MHD simulations where two adjacent and parallel gravitationally stratified coronal loops are slightly tilted, in accordance with the observed small POS crossings between rain strands.

The set-up we use here is inspired by refs. [39,40]. The initially magnetostatic loops include a chromosphere-like layer, a transition region and a million-degree corona, relaxed to a steady state by solving the 3D resistive MHD equations with the PLUTO code[41]. The MHD equations include thermal conduction and radiative losses, and incorporate an anomalous magnetic resistivity term that switches on to (otherwise) non-zero values whenever the current density exceeds a specific threshold (see Supplementary Information).

We impose a transient driver at the chromospheric footpoints of both loops that slowly drifts them in opposite directions, to generate a slight x-type misalignment in the corona. The rearrangement of the magnetic field in the corona leads to a steady increase of the misalignment angle θ_i between both loops, from 3° at $t \approx 180$ s to almost 8° at $t \approx 360$ s (Supplementary Fig. 19b), before slightly decreasing.

Near $t = 380$ s, the increase in the tilt angle produces an increase in the electric current between the loops that overcomes the threshold for the anomalous resistivity and diffusion of the magnetic field sets in (Supplementary Fig. 19a). At this time, the characteristic length L of the region in which the electric currents are larger than the threshold is about 0.3 Mm, the plasma velocity V is of the order of $50\,\mathrm{km\,s^{-1}}$ and the resistivity coefficient is $\eta_0 = 10^{14}\,\mathrm{cm^{-2}\,s^{-1}}$. This leads to a magnetic Reynolds number of

$$R_M = \frac{VL}{\eta_0} \approx 1. \quad (1)$$

In this regime, the timescales for the diffusion and advection of the magnetic field are similar, and magnetic reconnection sets in. Magnetic field lines change connectivity from one loop to the other, with a change of direction at the centre of the domain (the B_y component of the magnetic field grows up to 0.07 G before flipping sign after the reconnection). This changed topology leads to an enhanced magnetic tension in that region (Supplementary Fig. 20b), which begins to displace the plasma transversely. Accordingly, the velocity V_y of the plasma rapidly increases to well above $200\,\mathrm{km\,s^{-1}}$ (Supplementary Fig. 20c), which is much higher than any value previously found in the simulation.

Near the centre of the domain, the magnetic energy initially increases with the y component of the local magnetic field (Supplementary Fig. 19b). When the anomalous resistivity is triggered, the magnetic energy drops below the initial value, and the thermal and kinetic energies increase on a very similar timescale and to a similar magnitude (Supplementary Fig. 21a). The large variation in the magnetic and thermal energies is mainly due to driving two large flux tubes (leading to a large Poynting flux from the lower boundaries). On the other hand, the kinetic energy increase seems to be smaller because it is more localized and is partly converted into thermal energy during the plasma compression. This is associated with an average speed of $\sim 140\,\mathrm{km\,s^{-1}}$, whereas the plasma is accelerated locally up to $\sim 300\,\mathrm{km\,s^{-1}}$. We identify the localized regions near the centre of the domain where the plasma is accelerated to $200\,\mathrm{km\,s^{-1}}$ or more as jets (Fig. 5). The temperature experiences a jump of 3×10^6 K when the reconnection is triggered (Supplementary Fig. 21b). The outflow thermal energy rate is comparable to the inflow electromagnetic energy rate (Supplementary Fig. 21c). The value of the critical current above which the anomalous resistivity sets in does not influence the dynamics of the nanojet and the attained temperature (see Supplementary Information).

The region where the electric current is equal to the threshold to trigger the anomalous resistivity has an 'x' shape located between the two loops (Fig. 5b). The highest velocities are highly localized, where the region with $|V_y| \geq 190\,\mathrm{km\,s^{-1}}$ is a few megametres long (Fig. 5c). However, V_y velocities around $100\,\mathrm{km\,s^{-1}}$ are also found along the reconnected field lines to a distance half-way down the loop, indicating a strong transverse motion of the entire reconnecting strand. The high velocity region is adjacent to the reconnected magnetic field lines that show a curvature generating an outward magnetic tension near $z = 0$ (Supplementary Fig. 20). This configuration is not found before reconnection. The longitudinal velocities (V_z) are always below a few tens of kilometres per second. Hence, the reconnection triggers the highest velocities mostly along the y direction (that is, perpendicular to the guide magnetic field and coronal loop axes) and only minor motions along the loops.

Therefore, the numerical model leads to results with the same telltale signatures as the observed nanojets. On the other hand, the timescale of the changes and corresponding energy release is large due to the size of the flux tubes being driven. The changes occur on a timescale of 100 s, longer than the timescale of a single nanojet (15 s or less) but similar to that of the nanojet clusters. The localization of the jets in the numerical model is also roughly five times larger than that of a single nanojet, but similar to the width of the nanojet cluster. Although our model does not capture the exact conditions of the observed plasma (partially ionized, cool and dense), we consider that the same physics would occur in more detailed experiments. The differences from the numerical experiment—particularly the single and clustered manifestation of the nanojets at faster timescales and smaller length scales, accompanied by plasmoids—constitute a challenge for future numerical models of magnetic reconnection that can clarify the detailed physics of this process in the solar corona.

Data availability

The IRIS and Hinode observations used in the instrument data figures are available at https://bit.ly/3gcI2Wt. Other data used in this Article are available from the corresponding author on reasonable request.

Code availability

PLUTO is a modular Godunov-type code for solving mixed hyperbolic/parabolic systems of partial differential equations (conservation laws) targeting high Mach number flows in astrophysical fluid dynamics. Equations are discretized and solved on a structured mesh that can be either static or adaptive through the Adaptice Mesh Refinement (AMR) interface. PLUTO is distributed freely under the GNU general public license and can be downloaded at http://plutocode.ph.unito.it/.

Received: 31 May 2019; Accepted: 23 July 2020;
Published online: 21 September 2020

References

1. Parker, E. N. Nanoflares and the solar X-ray corona. *Astrophys. J.* **330**, 474–479 (1988).
2. Cargill, P. J. Some implications of the nanoflare concept. *Astrophys. J.* **422**, 381–393 (1994).
3. Rappazzo, A. F., Velli, M., Einaudi, G. & Dahlburg, R. B. Nonlinear dynamics of the Parker scenario for coronal heating. *Astrophys. J.* **677**, 1348–1366 (2008).
4. Biskamp, D. Magnetic reconnection via current sheets. *Phys. Fluids* **29**, 1520–1531 (1986).
5. Zweibel, E. G. & Yamada, M. Magnetic reconnection in astrophysical and laboratory plasmas. *Annu. Rev. Astron. Astrophys.* **47**, 291–332 (2009).
6. Bhattacharjee, A., Huang, Y.-M., Yang, H. & Rogers, B. Fast reconnection in high-Lundquist-number plasmas due to the plasmoid instability. *Phys. Plasmas* **16**, 112102 (2009).
7. Cirtain, J. W. et al. Energy release in the solar corona from spatially resolved magnetic braids. *Nature* **493**, 501–503 (2013).
8. Testa, P. et al. Observing coronal nanoflares in active region moss. *Astrophys. J. Lett.* **770**, L1 (2013).
9. Testa, P. et al. Evidence of nonthermal particles in coronal loops heated impulsively by nanoflares. *Science* **346**, 1255724 (2014).
10. Testa, P., Polito, V. & Pontieu, B. D. IRIS observations of short-term variability in moss associated with transient hot coronal loops. *Astrophys. J.* **889**, 124 (2020).
11. Tian, H. et al. Observations of subarcsecond bright dots in the transition region above sunspots with the Interface Region Imaging Spectrograph. *Astrophys. J. Lett.* **790**, L29 (2014).
12. Bai, X. Y. et al. Multi-wavelength observations of a subarcsecond penumbral transient brightening event. *Astrophys. J.* **823**, 60 (2016).
13. Ishikawa, S. et al. Detection of nanoflare-heated plasma in the solar corona by the FOXSI-2 sounding rocket. *Nat. Astron.* **1**, 771–774 (2017).
14. Moriyasu, S., Kudoh, T., Yokoyama, T. & Shibata, K. The nonlinear Alfvén wave model for solar coronal heating and nanoflares. *Astrophys. J. Lett.* **601**, L107–L110 (2004).
15. Antolin, P., Shibata, K., Kudoh, T., Shiota, D. & Brooks, D. Predicting observational signatures of coronal heating by Alfvén waves and nanoflares. *Astrophys. J.* **688**, 669–682 (2008).
16. Sterling, A. C., Moore, R. L., Falconer, D. A. & Adams, M. Small-scale filament eruptions as the driver of X-ray jets in solar coronal holes. *Nature* **523**, 437–440 (2015).
17. Takasao, S., Asai, A., Isobe, H. & Shibata, K. Simultaneous observation of reconnection inflow and outflow associated with the 2010 August 18 solar flare. *Astrophys. J. Lett.* **745**, L6 (2012).
18. Reale, F., Peres, G., Serio, S., DeLuca, E. E. & Golub, L. A brightening coronal loop observed by TRACE. I: morphology and evolution. *Astrophys. J.* **535**, 412–422 (2000).
19. Reale, F. et al. A brightening coronal loop observed by TRACE. II: loop modeling and constraints on heating. *Astrophys. J.* **535**, 423–437 (2000).

20. Reid, A. et al. Ellerman bombs with jets: cause and effect. *Astrophys. J.* **805**, 64 (2015).
21. Rouppe van der Voort, L. et al. Intermittent reconnection and plasmoids in UV bursts in the low solar atmosphere. *Astrophys. J. Lett.* **851**, L6 (2017).
22. Katsukawa, Y. et al. Small-scale jetlike features in penumbral chromospheres. *Science* **318**, 1594–1597 (2007).
23. Shibata, K. et al. Chromospheric anemone jets as evidence of ubiquitous reconnection. *Science* **318**, 1591–1594 (2007).
24. Lu, E. T., Hamilton, R. J., McTiernan, J. M. & Bromund, K. R. Solar flares and avalanches in driven dissipative systems. *Astrophys. J.* **412**, 841–852 (1993).
25. Charbonneau, P., McIntosh, S. W., Liu, H.-L. & Bogdan, T. J. Avalanche models for solar flares (Invited Review). *Sol. Phys.* **203**, 321–353 (2001).
26. Aschwanden, M. J. et al. 25 years of self-organized criticality: solar and astrophysics. *Space Sci. Rev.* **198**, 47–166 (2016).
27. Lemen, J. R. et al. The Atmospheric Imaging Assembly (AIA) on the Solar Dynamics Observatory (SDO). *Sol. Phys.* **275**, 17–40 (2012).
28. De Pontieu, B. et al. The Interface Region Imaging Spectrograph (IRIS). *Sol. Phys.* **289**, 2733–2779 (2014).
29. Suematsu, Y. et al. The Solar Optical Telescope of Solar-B (Hinode): the optical telescope assembly. *Sol. Phys.* **249**, 197–220 (2008).
30. Tsuneta, S. et al. The Solar Optical Telescope for the Hinode mission: an overview. *Sol. Phys.* **249**, 167–196 (2008).
31. Antolin, P., Pagano, P., De Moortel, I. & Nakariakov, V. M. In situ generation of transverse magnetohydrodynamic waves from colliding flows in the solar corona. *Astrophys. J. Lett.* **861**, L15 (2018).
32. Antolin, P., Vissers, G., Pereira, T. M. D., Rouppe van der Voort, L. & Scullion, E. The multithermal and multi-stranded nature of coronal rain. *Astrophys. J.* **806**, 81 (2015).
33. Hood, A. W., Cargill, P. J., Browning, P. K. & Tam, K. V. An MHD avalanche in a multi-threaded coronal loop. *Astrophys. J.* **817**, 5 (2016).
34. Keppens, R. & Xia, C. The dynamics of funnel prominences. *Astrophys. J.* **789**, 22 (2014).
35. Martínez-Sykora, J. et al. Ion-neutral interactions and nonequilibrium ionization in the solar chromosphere. *Astrophys. J.* **889**, 95 (2020).
36. Cheung, M. C. M. et al. Thermal diagnostics with the atmospheric imaging assembly on board the Solar Dynamics Observatory: a validated method for differential emission measure inversions. *Astrophys. J.* **807**, 143 (2015).
37. Huang, Y.-M. & Bhattacharjee, A. Distribution of plasmoids in high-Lundquist-number magnetic reconnection. *Phys. Rev. Lett.* **109**, 265002 (2012).
38. Chen, H., Zhang, J., Ma, S., Yan, X. & Xue, J. Solar tornadoes triggered by interaction between filaments and EUV jets. *Astrophys. J. Lett.* **841**, L13 (2017).
39. Petralia, A., Reale, F., Orlando, S. & Testa, P. Bright hot impacts by erupted fragments falling back on the sun: magnetic channelling. *Astrophys. J.* **832**, 2 (2016).
40. Petralia, A., Reale, F. & Testa, P. Guided flows in coronal magnetic flux tubes. *Astron. Astrophys.* **609**, A18 (2018).
41. Mignone, A. et al. The PLUTO code for adaptive mesh computations in astrophysical fluid dynamics. *Astrophys. J. Suppl.* **198**, 7 (2012).

Acknowledgements

P.A. acknowledges STFC support from grant numbers ST/R004285/2 and ST/T000384/1 and support from the International Space Science Institute, Bern, Switzerland to the International Teams on 'Implications for coronal heating and magnetic fields from coronal rain observations and modeling' and 'Observed Multi-Scale Variability of Coronal Loops as a Probe of Coronal Heating'. This project has received funding from the European Research Council (ERC) under the European Union's Horizon 2020 research and innovation programme (grant agreement no. 647214). P.T. was also supported by contracts 8100002705 and SP02H1701R from Lockheed-Martin to the Smithsonian Astrophysical Observatory (SAO), and NASA contract NNM07AB07C to the SAO. P.A. thanks I. De Moortel, R. Rutten and B. De Pontieu for valuable discussion and J. A. McLaughlin for the suggested name of the nanojet. Hinode is a Japanese mission developed and launched by ISAS/JAXA, with NAOJ as domestic partner and NASA and STFC (UK) as international partners. It is operated by these agencies in co-operation with ESA and NSC (Norway). IRIS is a NASA small explorer mission developed and operated by LMSAL with mission operations executed at NASA Ames Research Center and major contributions to downlink communications funded by ESA and the Norwegian Space Centre. SDO is part of NASA's Living With a Star Program. All data used in this work are publicly available through the websites of the respective solar missions. This work used the DiRAC@Durham facility managed by the Institute for Computational Cosmology on behalf of the STFC DiRAC HPC Facility (https://www.dirac.ac.uk). The DiRAC@Durham equipment was funded by BEIS capital funding via STFC capital grants ST/P002293/1 and ST/R002371/1, Durham University and STFC operations grant ST/R000832/1. The DiRAC component of CSD3 was funded by BEIS capital funding via STFC capital grants ST/P002307/1 and ST/R002452/1 and STFC operations grant ST/R00689X/1. DiRAC is part of the National e- Infrastructure.

Author contributions

P.A. was responsible for the planning, coordination, image processing, analysis of the observations and writing of most of the manuscript. P.P. was responsible for the numerical simulations and wrote the analysis of the numerical results. P.T. was responsible for the differential emission measure analysis and wrote the corresponding section in the manuscript. A.P. and F.R. provided the numerical code and the initial condition for the numerical simulation. A.P., F.R. and P.T. also provided feedback on the analysis of the results and the writing of the manuscript.

Competing interests

The authors declare no competing interests.

Additional information

Extended data is available for this paper at https://doi.org/10.1038/s41550-020-1199-8.

Supplementary information is available for this paper at https://doi.org/10.1038/s41550-020-1199-8.

Correspondence and requests for materials should be addressed to P.A.

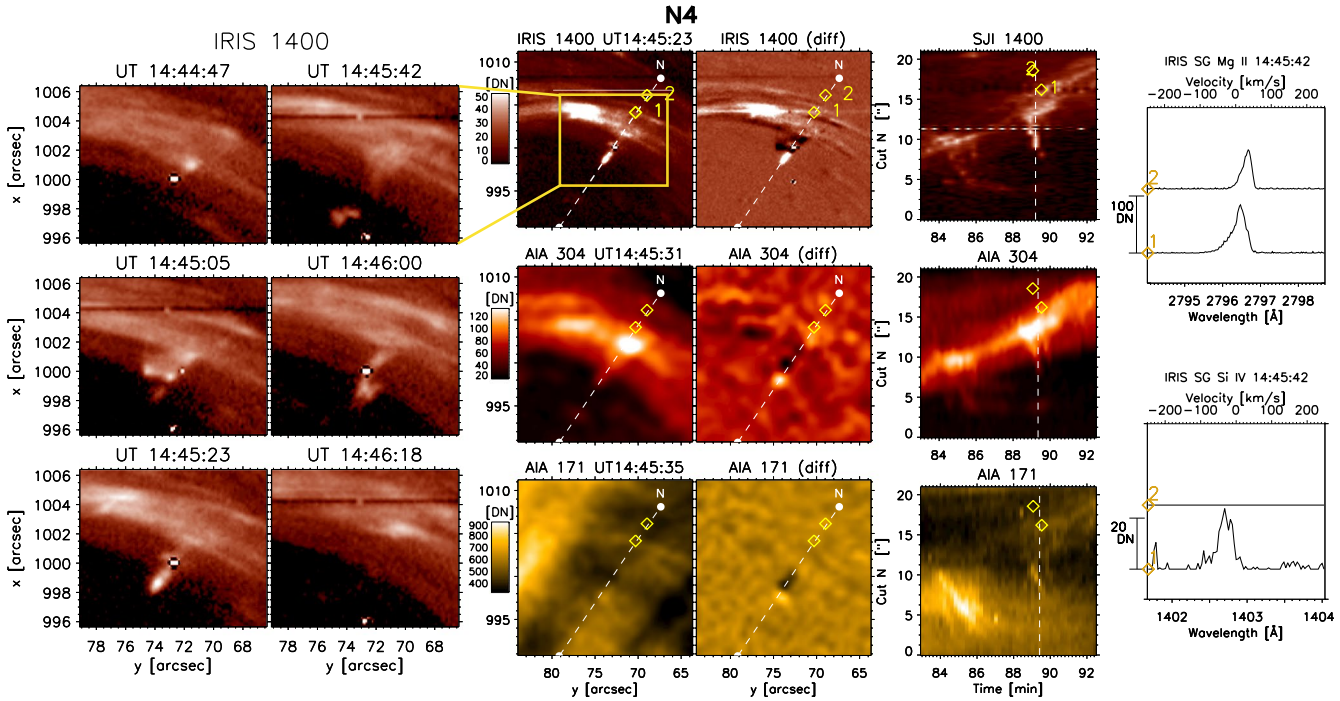

Extended Data Fig. 1 | Nanojet N4. Snapshots of nanojet N4 and the time–distance diagram along the nanojet axis (see Fig. 2 for further details). Part of the process is captured by the IRIS slit at position 1 (marked in the figure). Note the rapid succession of 2 nanojets, whose slopes in the time–distance diagrams are seen in all channels. To spatially and temporally locate this nanojet within the global loop structure and during the loop expansion see Extended Data Figs. 5 and 6, respectively. See Supplementary Video 5.

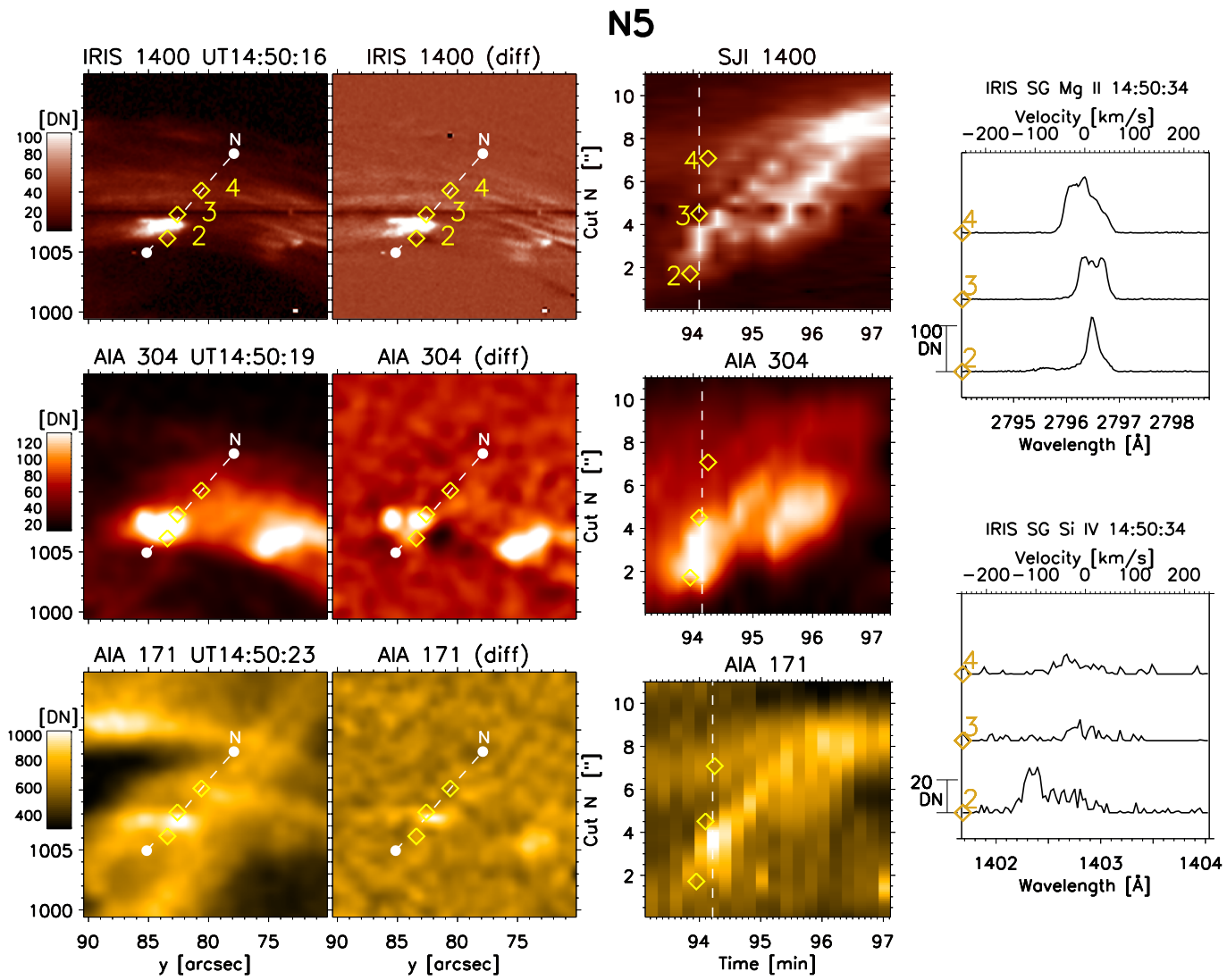

Extended Data Fig. 2 | Nanojet N5. Snapshots of nanojet N5 and the time–distance diagram along the nanojet axis (see Fig. 2 for further details). The IRIS slit at position 2 (marked in the figure) captures the strongest feature, with a Doppler peak at ≈ −120 km s^{-1} and a long velocity tail down to ≈ −10 km s^{-1}. Positions 3 and 4 capture the subsequent evolution. Note that the large blueshift seen in the Si IV line is almost absent in the Mg II line. To spatially and temporally locate this nanojet within the global loop structure and during the loop expansion see Extended Data Figs. 5 and 6, respectively. See Supplementary Video 6.

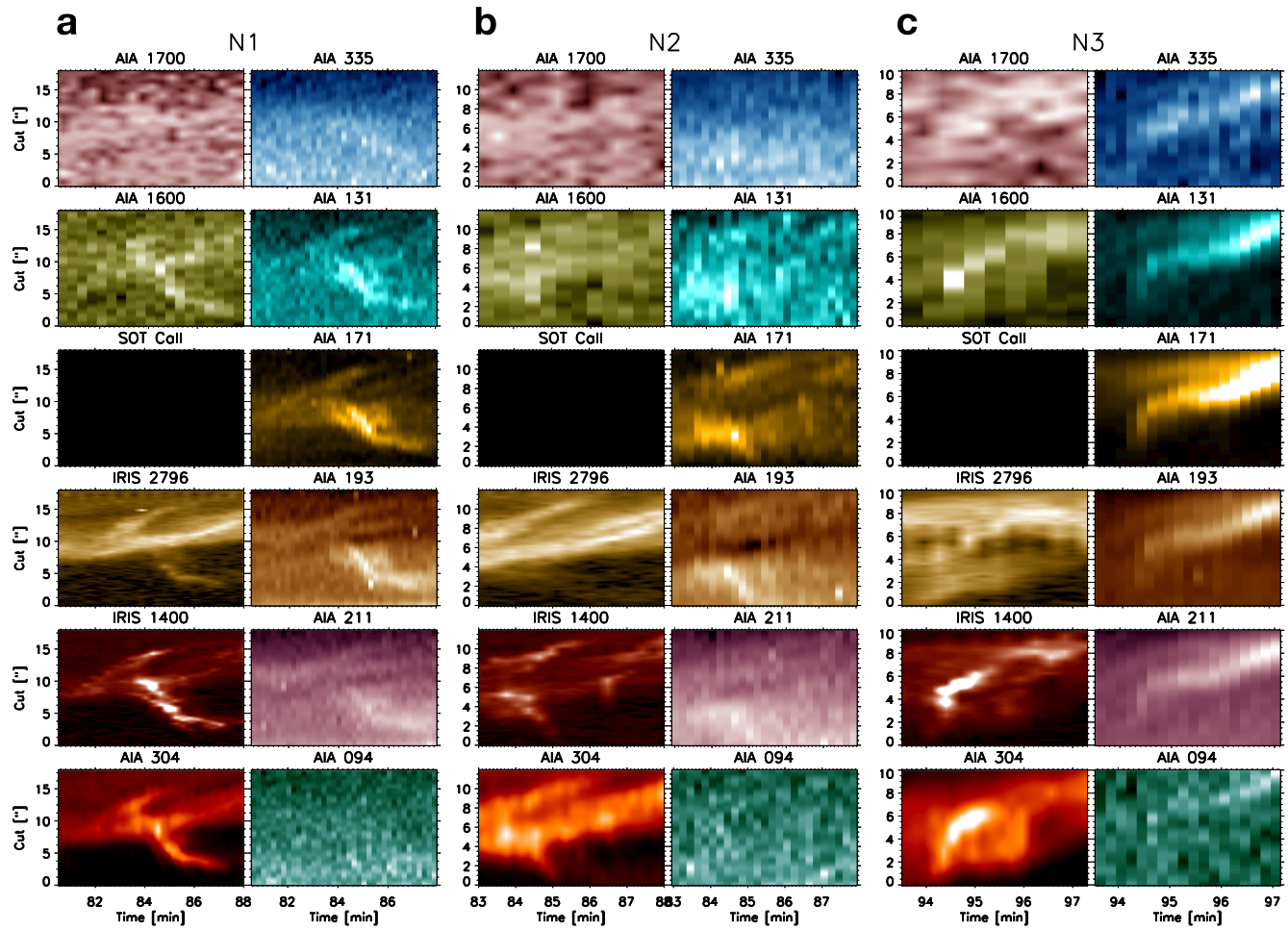

Extended Data Fig. 3 | EUV signatures of nanojets N1, N2 and N3. a–**c**, Time–distance maps in all AIA and IRIS channels (SOT stopped observing at this time) along cuts corresponding to the axis of nanojets N1 (**a**), N2 (**b**) and N3 (**c**) shown, respectively, in Figs. 2, 3 and 4. The temporal and spatial extent shown is the same as that of the time–distance diagrams shown in those figures. The N1 and N2 cuts trace part of the first clustered appearance of nanojets and the ejection of plasmoids. All cuts show an intensity enhancement that is similar across most EUV channels, indicating very fast and substantial heating.

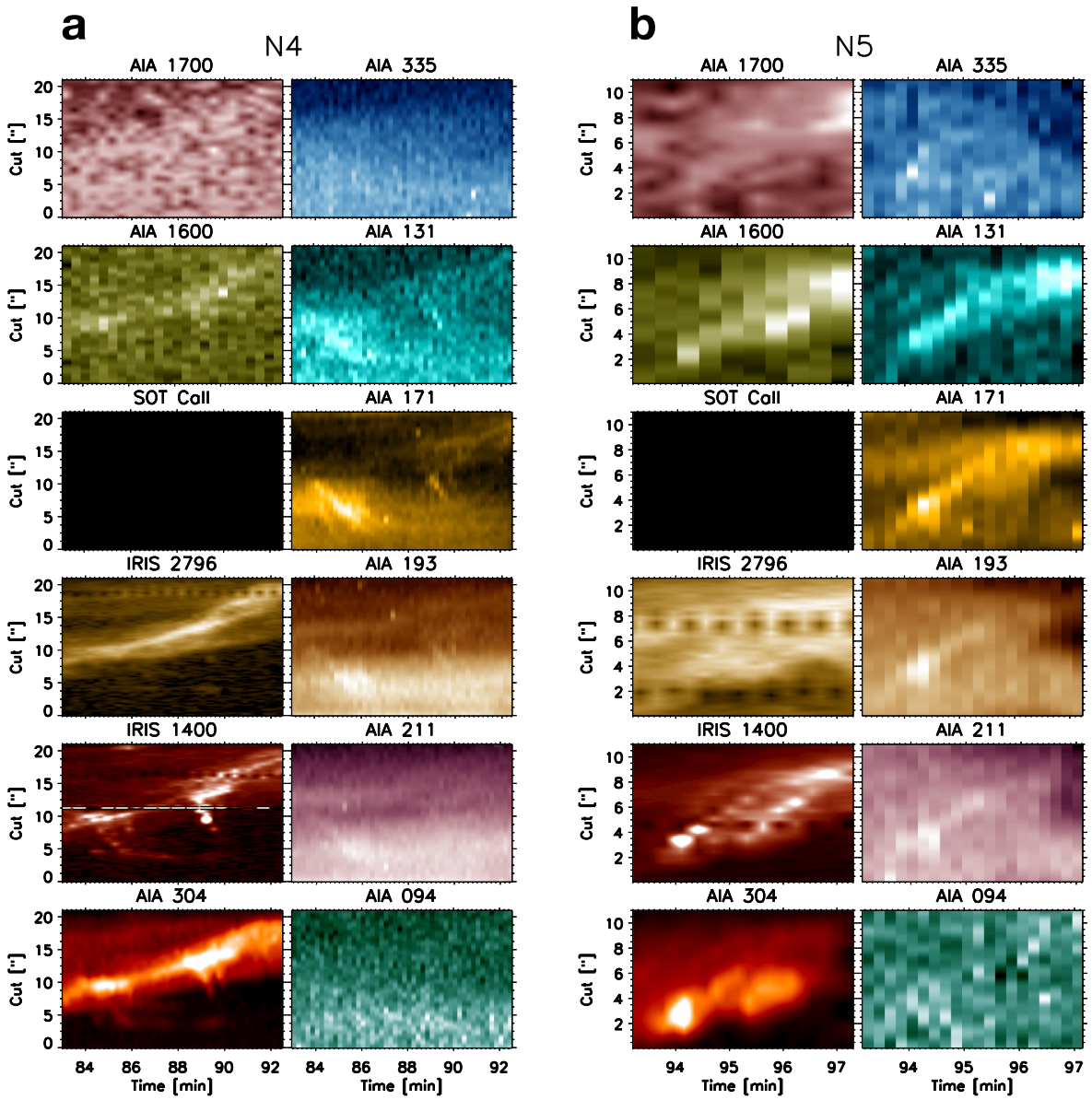

Extended Data Fig. 4 | EUV signatures of nanojets N4 and N5. a,**b**, Time–distance maps in all AIA and IRIS channels (SOT stopped observing at this time) along cuts corresponding to the axis of nanojets N4 (**a**) and N5 (**b**), shown, respectively, in Extended Data Figs. 1 and 2. The temporal and spatial extent shown is the same as that of the time–distance diagrams shown in those figures.

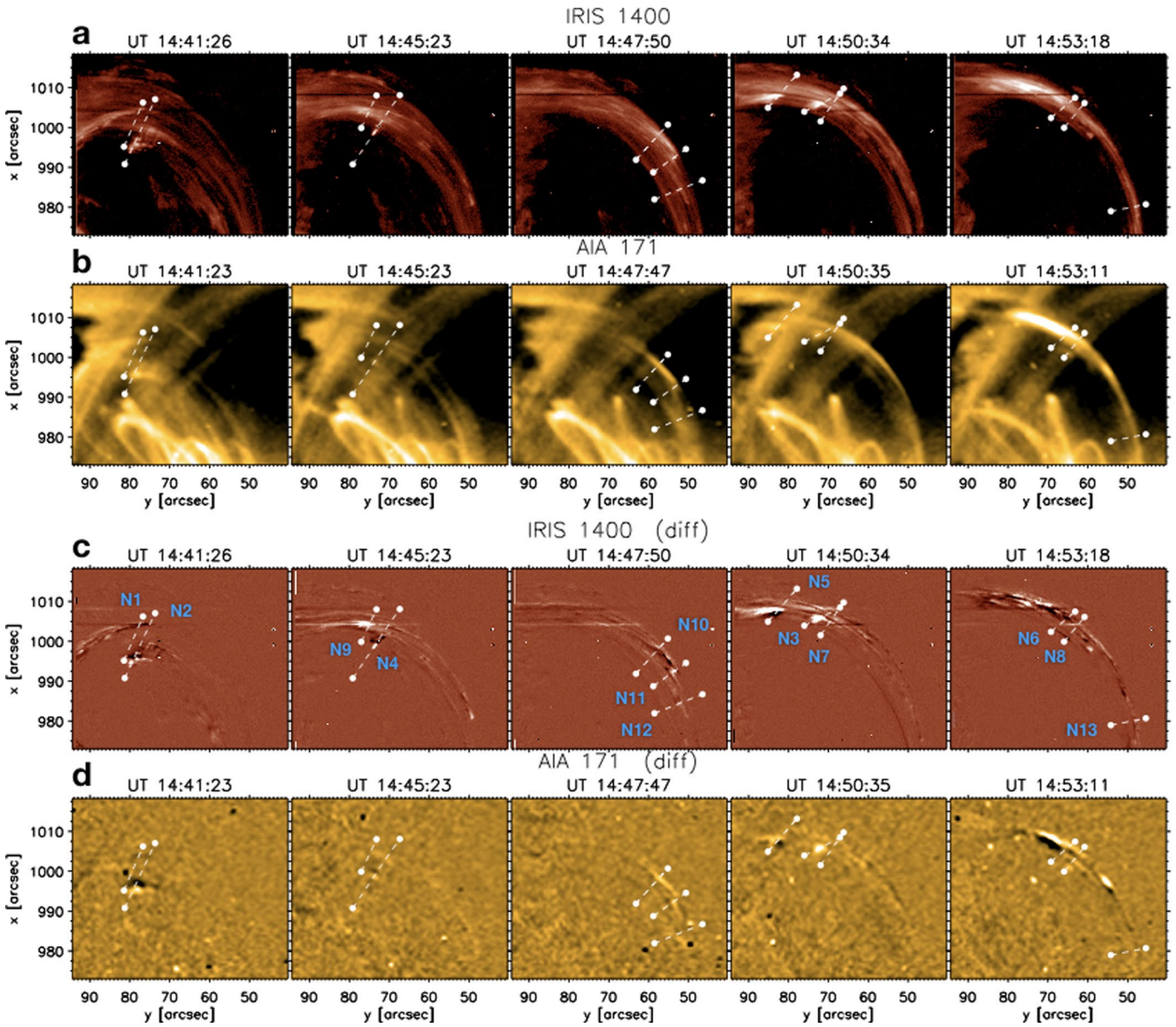

Extended Data Fig. 5 | Formation of strands. a–**d**, Five moments during the expansion period of the loop are selected that show the global evolution of the structure in the IRIS 1,400 Å channel (**a**) and AIA 171 Å channel (**b**), together with the corresponding running difference images in **c** and **d**. The cuts for the nanojets 'N1' to 'N13' are overlaid in groups, according to their time of occurrence. See Extended Data Fig. 6 for a more precise time location of these nanojets during the evolution. Note the formation of very fine and long coronal strands that originate from the nanojets.

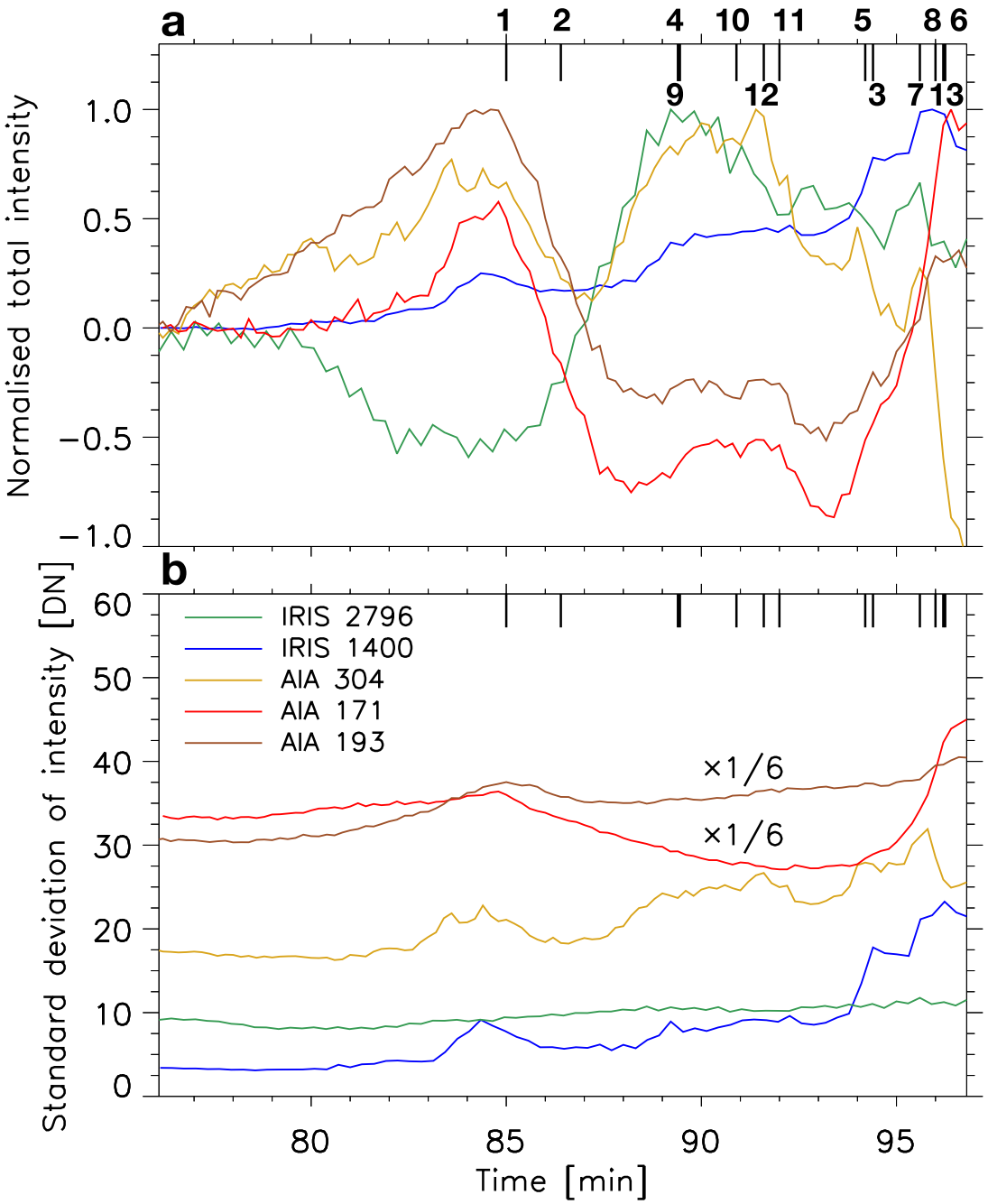

Extended Data Fig. 6 | UV & EUV lightcurves. a, A curved slab containing the loop of interest is selected (avoiding most bright structures along the LOS present in the hot channels), and the total over the slab of the intensity relative to a time prior to the loop expansion ($t = 76$ min) is shown for the IRIS channels and AIA 304 Å, 171 Å and 193 Å channels, normalised to their maxima over the last 22min of observation. The expansion of the loop starts from $t \approx 84$ min. We mark with a small vertical line and corresponding nanojet number the location in time of the nanojets 'N1' to 'N13'. **b**, Standard deviation of the total intensity calculated in **a**. The unit is DN, a representative of the number of photons (see Fig. 2 for details). Note that the values for AIA 171 and 193 have been divided by 6 in order to fit in the same axis. See the legend in the figure for the colour corresponding to each channel. The level of noise in each channel, as measured from the standard deviation over a quiet region off-limb in the IRIS 1,400, 2,796 and AIA 304, 171, 193 is, respectively, 1, 1.1, 1.4, 18.9 and 65.6 DN.

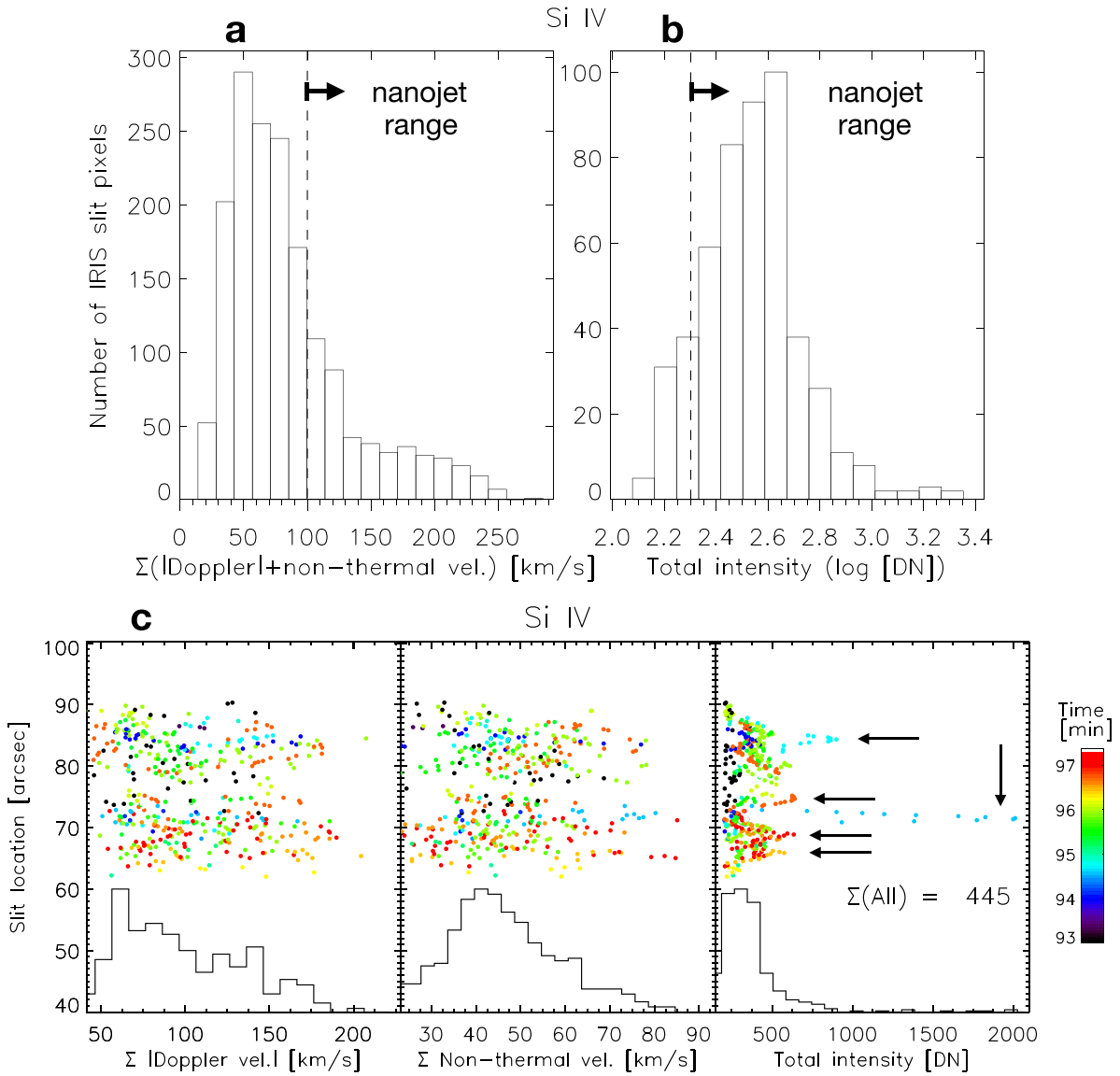

Extended Data Fig. 7 | Statistics of nanojets. a, Total velocity distribution of IRIS slit pixels having a total intensity above 200 DN (equal to ≈ 1.4 times the total intensity average during the quiet, non-expansion period of the loop). The total velocity is defined as the sum in absolute value of all Doppler components and non-thermal velocities for each pixel. **b**, Total intensity distribution of IRIS slit pixels having a total velocity higher than 100 km s^{-1}. The slit pixels corresponding to the nanojets are defined as those having both a total intensity higher than 200 DN and a total velocity larger than 100 km s^{-1} (both ranges are marked by a vertical dashed line in the top histograms). **c**, Distribution of the nanojet pixels along the slit and for a time interval focusing on the last 4 min of observation (time in which the slit captures the nanojets best). The time evolution is shown with different colours. The total number of nanojet pixels within this time interval is 436. Histograms for each quantity are shown at the bottom of each plot. Note that the nanojets are characterised by increases in intensity, Doppler velocity and non-thermal velocity that are very localised in time and space. A few of the nanojets are marked with arrows.

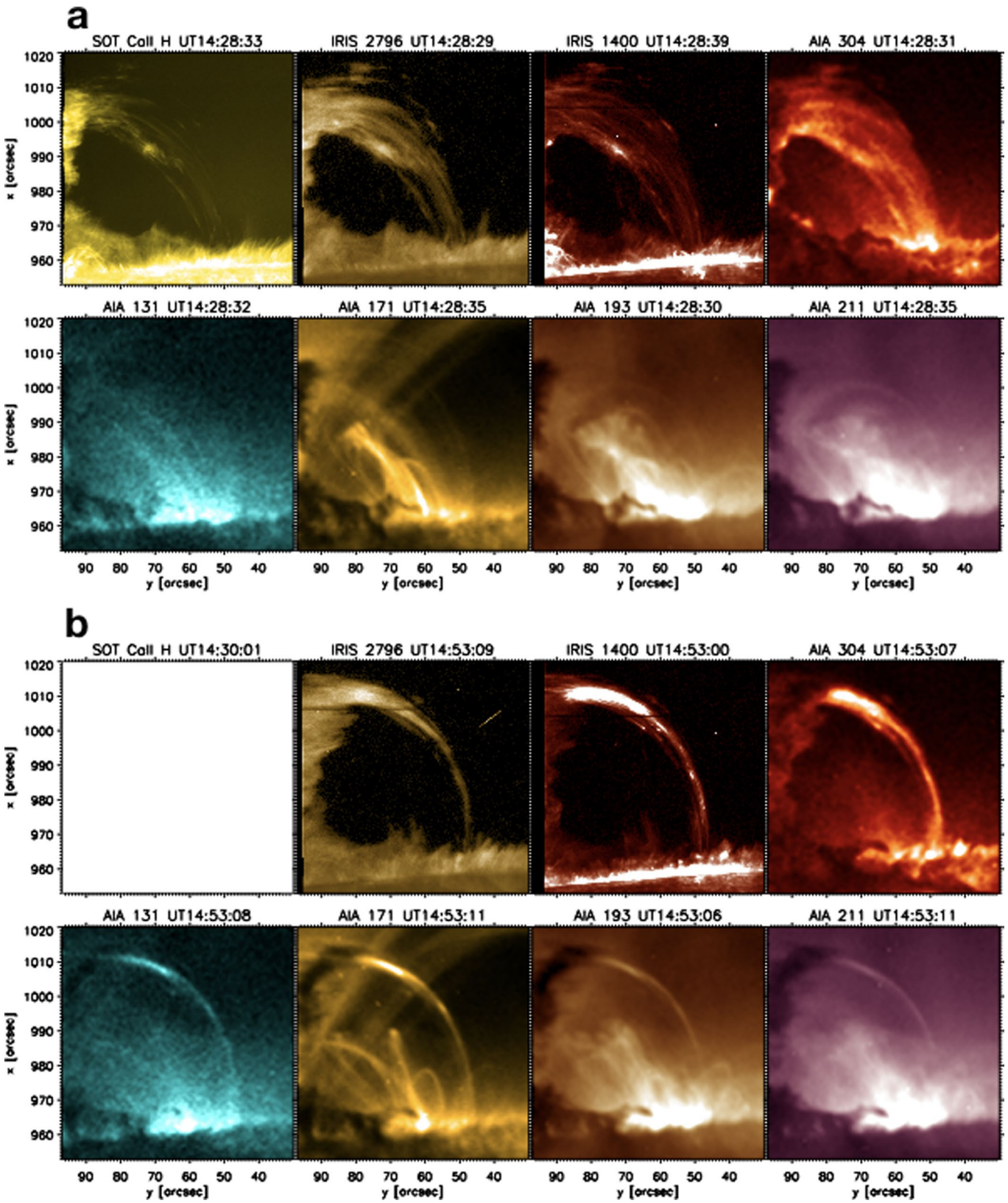

Extended Data Fig. 8 | Multi-wavelength view of the coronal structure with Hinode/SOT, IRIS and SDO/AIA. a, From top left to bottom right we show in order of increasing temperature formation, the common FOV of the coordinated observation at the same time shown in Fig. 1. Chromospheric temperatures are represented by the SOT Ca II H and IRIS 2,796 Å channels ($\log T \approx 4 - 4.2$). Lower transition region temperatures are represented by IRIS 1,400 Å and AIA 304 Å ($\log T \approx 4.8 - 5$). Upper transition region temperatures are represented by AIA 131 Å and 171 Å ($\log T \approx 5.7 - 5.9$). Coronal temperatures are best observed by AIA 193 Å and 211 Å ($\log T \approx 6.2 - 6.3$). A radial filter has been applied to the SOT, IRIS 2,796 Å and IRIS 1,400 Å images to decrease the disk intensity and to make the off-limb features more visible.**b**, Same as in **a** but at the last IRIS observation time (SOT has stopped observing at this time). Note the appearance of the coronal loop following the occurrence of nanojets. See Supplementary Video 7.

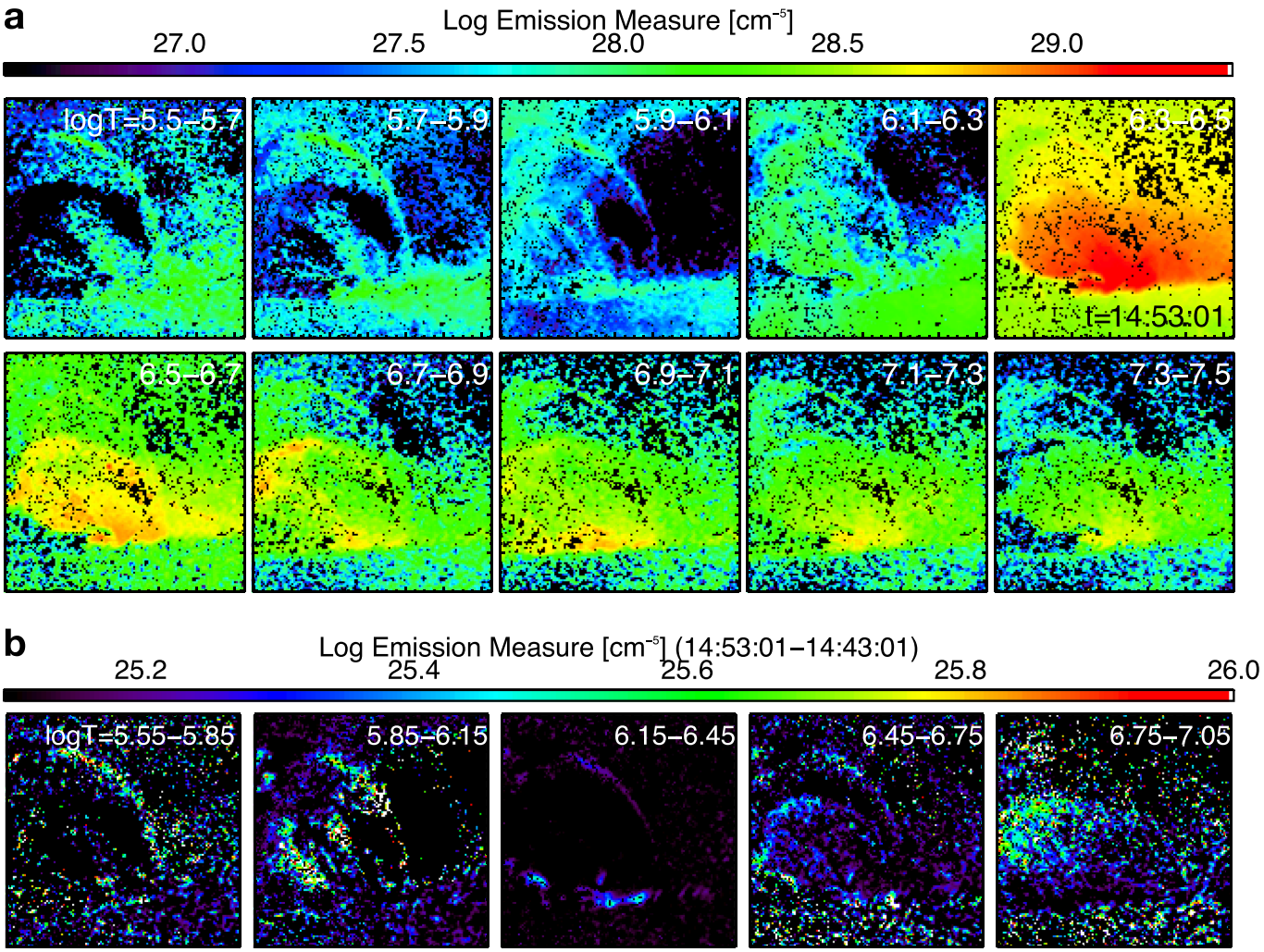

Extended Data Fig. 9 | Hot plasma emission measure in the loop. A DEM analysis is performed (see Methods) for which the temperature range is binned in intervals of $\log T = 0.2$. The FOV is the same as in Extended Data Fig. 8. **a**, A time towards the end of the loop expansion is selected ($t = 96.8$min) and the emission measure of the region for each bin is shown. Note the presence of hot plasma along the loop at temperatures of $\log T = 6.3 - 6.5$ (and possibly at higher temperatures as well). See Supplementary Video 8. **b**, To see better the appearance of this hot component in the loop the difference between the same snapshot as in **a** and a snapshot 10 min before is shown. The bins are regrouped to temperature widths of $\log T = 0.3$ for better visualisation. Note the distinct appearance of plasma at $\log T = 6.15 - 6.45$ and possibly also at $\log T = 6.45 - 6.75$.

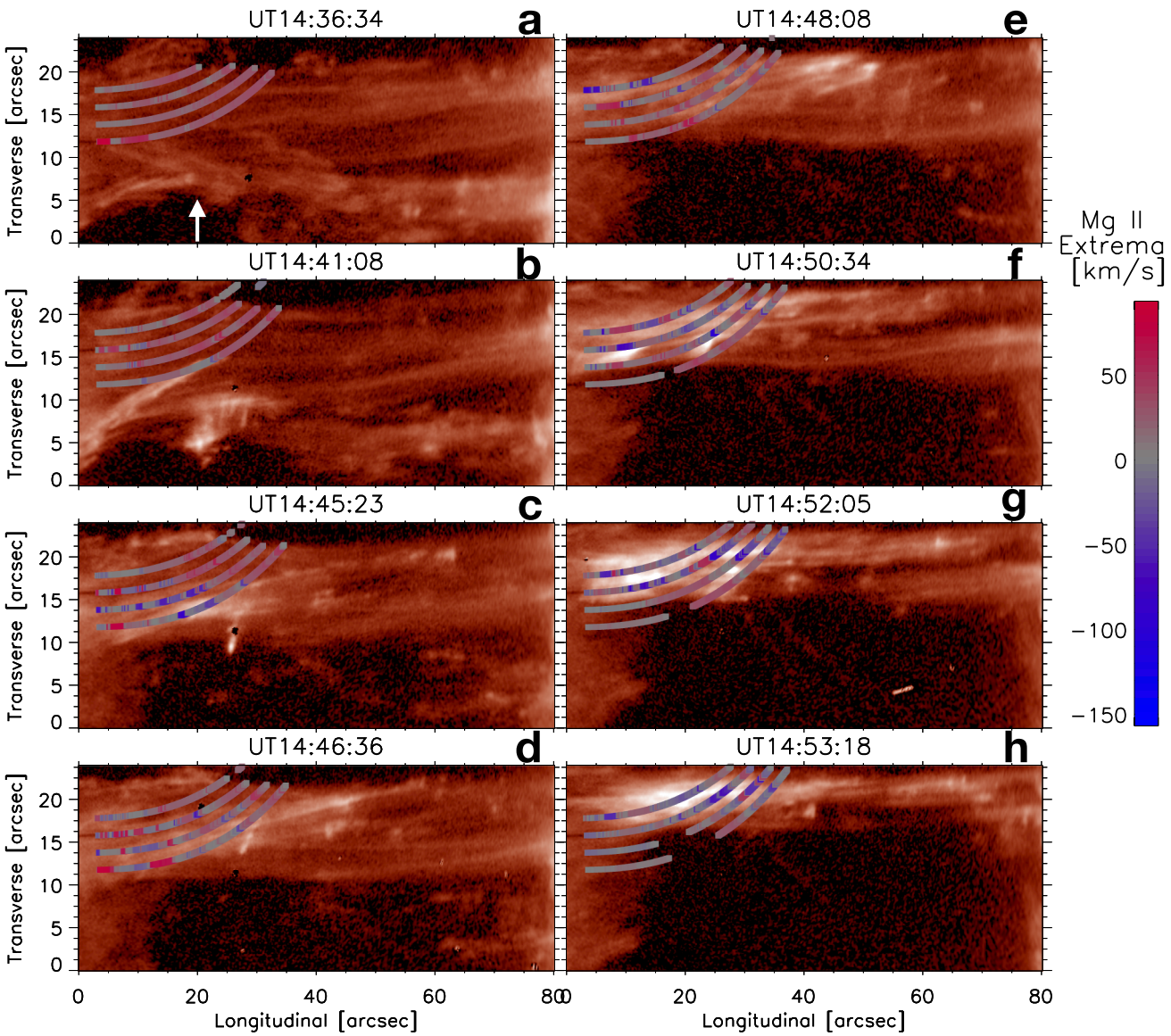

Extended Data Fig. 10 | Evolution of twist and braiding along the loop. A slab containing the loop is selected and the slab is interpolated into a rectangle in order to eliminate the loop curvature and better observe the presence of twist (*x* and *y* scales are different in the image). Several times during the expansion of the loop are selected and the Mg II k Doppler velocity (extrema among the multiple components at each pixel) measured from the IRIS slit is overlaid. The evolution goes from panels **a** to **h**. **a** shows the state of the loop just prior to the loop expansion. Note the presence of braiding. Particularly, 2 rain strands can be seen intersecting each other in the POS (white arrow in panel). Minutes later, **b** shows that one of the 2 intersecting strands has brightened and moved rapidly outward (and is blueshifted, contrary to the rest of the loop), while the other strand exhibits the clustered appearance of nanojets and plasmoid ejections. The following snapshots (**c** to **h**) indicate the rapid outward motion of the strands, local brightening events and the gradual reduction of twist and braiding along the loop. During this motion the strands at the lower part of the loop are on average redshifted while the upper part of the loop is blueshifted, suggesting an untwisting motion sketched in Supplementary Fig. 14. See Supplementary Video 9.